ISSN: 3144-1890

Wissen PUBLICATION GROUP

Journal of
Advanced Physics and Interdisciplinary Science

Research Article

Volume: 1 | Isssue: 1 | October 2026 | Pages 01–17

Construction of 3D Structures of Superconductivity Compounds Which May Possess Extremely Elevated Critical Temperatures

Clifford M Krowne, Emeritus

[1]Materials Physics & Chemistry Section, Materials and Sensors Branch, Material Science & Technology Division, and Microwave Circuits & Electromagnetic Theory Sections, Microwave Technology & Electromagnetics Branches, Electronics Science & Technology Division, Naval Research Laboratory, Washington, DC 20375, United States of America

[2]Chief Research Scientific Officer, Ashlawn Energy, LLC, 710 Resende Road, Bldg. 199, Webster, New York 14580, United States of America

***Corresponding Author:** Clifford M. Krowne, Materials Physics & Chemistry Section, Materials and Sensors Branch, Material Science & Technology Division, and Microwave Circuits & Electromagnetic Theory Sections, Microwave Technology & Electromagnetics Branches, Electronics Science & Technology Division, Naval Research Laboratory, Washington, DC 20375, United States of America.

Submitted: 09 October 2026 **Accepted:** 14 October 2026 **Published:** 23 October 2026

Citation: Krowne, C.M. (2026). Construction of 3D Structures of Superconductivity Compounds Which May Possess Extremely Elevated Critical Temperatures. Journal of Advanced Physics and Interdisciplinary Science, 1(1), 01-17. DOI: https://doi.org/10.67927/JAdvPhysInterdiscipSci/2026(1)108.

Abstract

Here are presented thoughts on how to construct 3D structure compound superconductors which may possess extremely high critical temperatures T_C. The solid-state chemistry employed to get to these compounds will be addressed too. Orbital character of the electrons associated with particular atoms, sub-unit cell crystal structures evidenced by looking at known unit cell crystal structures, insights into which parts of the sub-structure may provide carriers to the 1D, 2D or 3D transport pipes, sheets or tunnels, valence states of atoms, deficiency or excess atom dopants to enhance or assist carrier provision, all are addressed. Because the exchange energy compared to $k_B T_C$ may be significant in the moderate or strong coupling condition, new formulas for T_C and superconductor gap Δ , are developed to handle this contingency. Finally, in view of the detailed examination of prior unit cell superconductor crystal structures, metamaterial crystal structures are proposed, which may help elevate T_C.

Keywords: Superconductivity Compounds, 3D Structures, Cell Crystal Structures.

Introduction

Approach in this presentation is to provide new ideas on how to construct appropriate unit cell crystal structures that may provide a pathway to super high superconducting critical temperatures T_C. There are several ways to construct these new SC unit cell structures. One way is to adopt previous sub-cell crystal structures, and place them in new arrangements. Another way is to consider stacking them to increase their numbers, and this stacking could be done vertically (z-direction), horizontally (xy-plane), or even diagonally (in face planes, or even as 3D vector directions). One may even consider metamaterial approaches, developed later. Table 1 presents some elemental, cuprate and pnictide superconducting atoms used in constructing the various superconducting materials. Shown are the atom valence states, electron orbital configurations, and the type of superconductor. It is apparent that the valence states are related to the electron orbital configurations. One sees that some of the atoms may take on many possible valence states, which allows many possible compound constructions. It is expected that those various valence states adopted will also affect the local crystallographic bond angles, as well as affect the overall unit cell.

Table 1: Valence States, Electron Orbital Configurations, SC Type Where Atoms Used.

Atom in SC	Valence States	Electron Orbital Configuration	Type of SC
Al	+3 (+2,+1,0,-2,-1)	[Ne] $3s^2$ $3p^1$	Elemental; pnictide
Ga	+3 (-5 to +2)	[Ar] $3d^{10}$ $4s^2$ $4p^1$	Elemental
Hf	+4(-2 to +3;no -1)	[Xe] $4f^{14}$ $5d^2$ $6s^2$	Elemental
Hg	+1,+2 (-2)	[Xe] $4f^{14}$ $5d^{10}$ $6s^2$	Elemental; Cuprate
In	+3(-5t2,no-4,-3)	[Kr] $4d^{10}$ $5s^2$ $5p^1$	Elemental

Pb	+2+4(-4t+3n-3,2)	[Xe] $4f^{14}$ $5d^{10}$ $6s^2$ $6p^2$	Elemental
Re	+4+7(-3+6n-2)	[Xe] $4f^{14}$ $5d^5$ $6s^2$	Elemental
Ta	+5(-3t+4,no-2)	Xe] $4f^{14}$ $5d^3$ $6s^2$	Elemental
Tl	+1+3(-5,-2,-1,+2)	[Xe] $4f^{14}$ $5d^{10}$ $6s^2$ $6p^1$	Elemental; Cuprate
V	+5(-3 to +4,n-2)	[Ar] $3d^3$ $4s^2$	Elemental
Zr	+4(-2t+3,no-1)	[Kr] $4d^2$ $5s^2$	Elemental
Ba	+2 (+1)	[Xe] $6s^2$	Cuprate
Ca	+2(+1)	[Ar] $4s^2$	Cuprate; pnictide
Cu	+2(-2t+4)	[Ar] $3d^{10}$ $4s^1$	Cuprate
O	-2(-1to+2)	[He] $2s^2$ $2p^4$	Cuprate; pnictide
Y	+3(0 to +2)	[Kr] $4d^1$ $5s^2$	Cuprate
La	+3 (0,+1,+2)	[Xe] $5d^1$ $6s^2$	pnictide
Fe	+2,3(-2 to +7)	[Ar] $3d^6$ $4s^2$	pnictide
P	-3,3,5(-2 to +4)	[Ne] $3s^2$ $3p^3$	pnictide
As	-3,3,5(-2 to +4)	[Ar] $3d^{10}$ $4s^2$ $4p^3$	pnictide
Sm	+3 (0, +1, +2)	[Xe] $4f^6$ $6s^2$	pnictide
Pr	+3(0 to +5)	[Xe] $4f^3$ $6s^2$	pnictide
Si	-4,4(-3 to +3)	[Ne] $3s^2$ $3p^2$	pnictide
H	-1,+1	$1s^1$	pnictide
F	-1 (0)	[He] $2s^2$ $2p^5$	pnictide
Li	-1,+1	[He] $2s^1$	pnictide
Na	+1 (-1)	[Ne] $3s^1$	pnictide
Se	-2,2,4,6(-1,5)	[Ar] $3d^{10}$ $4s^2$ $4p^4$	pnictide
K	+1 (-1)	[Ar] $4s^1$	pnictide
Sr	+2 (+1)	[Kr] $5s^2$	pnictide

Moving on from Table 1, let's zoom in on some of the sub unit cell crystal structures encountered in the three classes of superconductors mentioned. We'll return eventually to include other superconductors like magnesium diboride, MgB_2, for example. Focus is of course, mostly directed toward the most promising superconductors already showing indications of high T_C potential. Therefore, first look at the pnictide and cuprate superconductors. A lot can be learned by taking a tour, so to speak, of the crystal structures of the pnictides first. In fact, one very interesting structure is the rather sophisticated pnictide $Ca_{10}(Pt_3As_8)(Fe_2As_2)_5$, examined by Ni et al., PNAS, 108 (45), E1019–E1026, 2011 [1]. The top panel of Figure 1 shows that the powder X-ray pattern for the10-3-8 phase can be described well by the determined crystal structure. For both compounds, the strongest reflections reveal a simple tetragonal basal plane sub cell with a_0~3.91Å as shown in the (hk0) single crystal X-ray diffraction pattern. However, weaker superlattice reflections, which correspond to a square structural supercell in the real space basal plane, oriented in the (210) direction, are also observed and lead to $a^* = b^* = a_0^*/\sqrt{5}$. This unusual superlattice condition is mathematically equivalent to that seen in $K_{0.8}Fe_{2-\delta}Se_2$ but arises from a completely different chemical mechanism—the commensurability condition of the (Pt_3As_8) or (Pt_4As_8) skutterudite layers with the Fe_2As_2 layers, rather than partial vacancy ordering. Inspection of the single crystal diffraction patterns in the c direction indicates that 10-4-8 phase has a primitive tetragonal cell, while the10-3-8 phase shows significant shifting of the stacking between neighboring layers. This layer shift results in a triclinic unit cell, despite the fact that the basal plane cell is essentially square—i.e., with a = b and γ ≈ 90°. One should realize, that either of these 10-n-8 crystals,

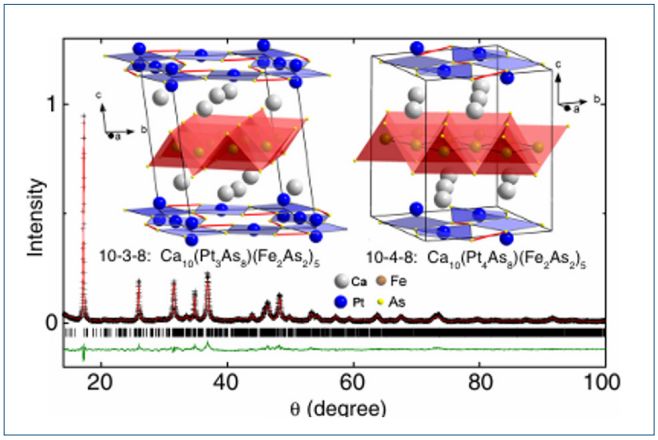


Figure 1: Shows a Calculated Crystal Structures for the 10-3-8 and 10-4-8 Pnictides (From Figure. 1 of [1]).

have relatively modest T_C's for the 10-3-8 phase, being T_C = 11 K, but much better and being more than double for the 10-4-8 phase, at T_C = 26 K. Related substructures are shown in Figure 2. It is known that the pnictide compounds can get up to T_C values around the mid-50s K. That is, T_C ≈55 K. This is a jump up from the 10-3-8 phase by a factor of 5.

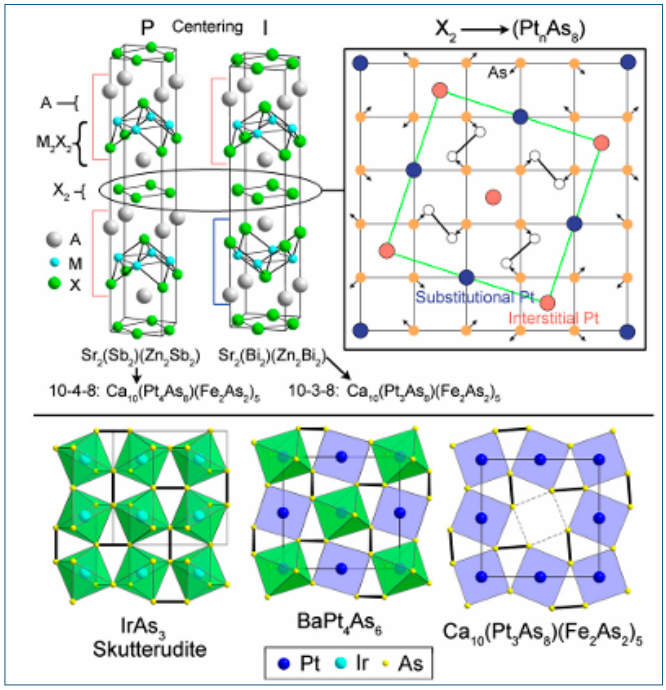


Figure 2: Crystal structures of $SrZnSb_2$ and $SrZnBi_2$, parent phases of the Ca-Fe-Pt-As superconductors (top left). Schematic of the change from X_2 layer in parent phases to Pt_nAs_8 skutterudite-like layers in the superconductors; center Pt interstitial only present in Pt_4As_8 layer (top right). Bottom, left to right, $IrAs_3$, $BaPt_4As_6$, and Pt_3As_8 intermediate layer in 10-3-8 superconducting phase. As-As bonds shown bold.

Further understanding of these substructures comes from inspection of Figure 3. Calculations leading to Figures. 1–3, arise from the orbital electron configurations detailed for some of the atoms found in superconductors listed in Table 1. But there are the four simpler pnictide iron Fe atom-based crystal structures of the 1111-, 122-, 111-, 11-types, shown in Table 2.

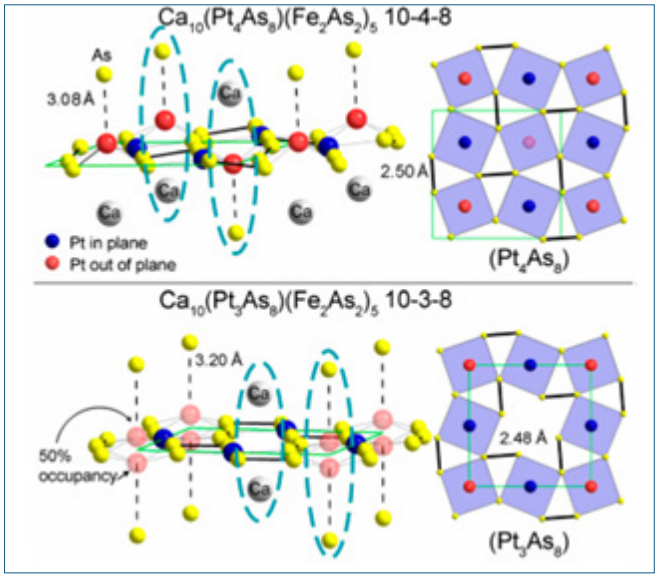


Figure 3: 2D 10-4-8 Pt-As plane, or the 2D 10-3-8 2D plane, with slightly out of plane Pt atoms, and the in-plane Pt atoms. Location of As atoms also shown, as are the Ca atoms.

Systematic Examination Some Basic Pnictides, Their Crystal Structures and Physical Properties

Table 2 lists four basic pnictides, which are instructive to examine for their crystal structures and physical prop-erties. Listed are the 1111-, 122-, 111-, and 11-pnictides.

Table 2: Basic Pnictide Super Conductors of the four Common Types 1111, 122, 111, and 11. In this Table, Ln Stands for Lanthanide Series Elements, While M Stands for Metal Atom.

Pnictide Type	Common Ex.	Crystal Struct.	Space Grp	Structure Prop.
1111	LaFeAsO	ZrCuSiAs	P4/nmm	$[LnO]^+$, $[FeAs]^-$ layers alternate
122	$BaFe_2As_2$	$ThCr_2Si_2$	I4/mmm	FeAs layers interspersed with M
111	LiFeAs	Cu_2Sb	P4/nmm	FeAs layers interspersed with Li
11	FeSe	PbO	P4/nmm	Only FeSe layers

The 1111-type of pnictide has the [LnO] spacer layer where Ln = lanthanide atom from the periodic table, act as an electron source for the [FeAs] layers, which is why they are superscripted respectively with a positive and negative signs in Table 2. Bonding arrangements for the Fe atoms which take the valence state +2, giving Fe^{2+}, bonds to four As atoms of valence state -3, giving As^{3-}. The result is formation of edge-sharing and corner tetrahedra $FeAs_4$. The 122-type of pnictide has FeAs layers separated from one another by single planes of alkaline metal ions with valence state +2, like Ba^{+2}, Ca^{+2}, Sr^{2+}, for example. At about T_{phase}=140 K , the crystal structure undergoes a symmetry change from tetragonal with space group I4/mmm to orthorhombic with space group F/mmm, and antiferromagnetic (AFM) ordering allowing spin density waves. Seemingly, superconductivity arises by atomic doping with substitutional atoms like K for Ba. The 111-type of pnictide has a tetragonal structure, like the compound Cu_2Sb, and does not need doping to get superconductivity. Bonding arrangement has one lithium-ion Li^{1+} bonded to five arsenide ions each of valence 3-, As^{3-} , forming distorted $LiAs_5$ trigonal pyramids. Common to the 1111-, 122-, and 111-types of pnictides, the Fe-As layers form a 2D square lattice. Pnictogen atoms, from group 15 of the Periodic Table of Elements namely, N, P, As, Sb, Bi, Mc, lie above or below the Fe-As plane. These atoms have the electron orbital configuration ns^2np^3, seen from Table 1, and typically form compounds utilizing the oxidations states of -3, +3, or +5. They can be nonmetals (N, P), metalloids (As, Sb), or metals (Bi).

Let's take a look at a 1111-type of pnictide, LaFeAsO, regarding its crystal structure in Figure. 4, adopted from Nomura [2]. Perspective view indicates the layered Fe-As structure. Distorted tetrahedrons of $FeAs_4$ are connected in an edge sharing manner to form the Fe-As layer. Top view of the crystal structure from c-direction. The inner square represents the unit cell in the

tetragonal phase (P4/nmm), while the outer square is that in the orthorhombic phase (Cmma). The unit cell of the orthorhombic phase rotates by 45° from that of the tetragonal phase and the lattice constants expands by √2, resulting in the increase in number of the chemical formula in a unit cell from 2 to 4.

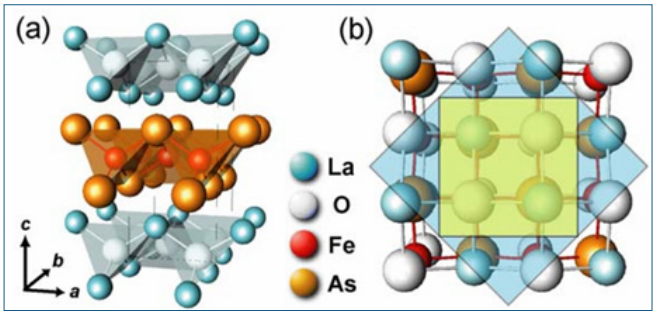


Figure 4: Crystal structure of LaFeAsO. (a) Perspective view indicates the layered Fe-As structure. (b) Top view of the crystal structure from c-direction. The inner square represents the unit cell in the tetragonal phase (P4/nmm). The outer square is that in the orthorhombic phase (Cmma). Taken from [2].

Of great interest is the spin ordering of the iron Fe atoms in the 1111-type of pnictides, because of their association with ferromagnetic (FM), or in the case of this class of compounds, antiferromagnetic (AFM) behavior. By experimental and density functional calculations (using the PW91 DFT), the 3d Fe electrons order in checkboard (alternating spin patterns in both 2D planar directions, the x- and y-directions, where $\vec{S} = s\hat{y}$),), or spin stripe patterns, seen in Fig. 5. In the tetragonal phase, the upper left-hand images represent AF1 (checkerboard type; T phase) of spin ordering, whereas the upper middle AF2a and right-hand AF2b images represent spin stripe type (O phase) configurations. Under relaxation to the orthorhombic phase, the lower images represent the spin configurations of AF1, AF2a and AF2b. The a-axis (x direction) is longer than the b-axis (y direction) in O_1 and vice versa in O_2.

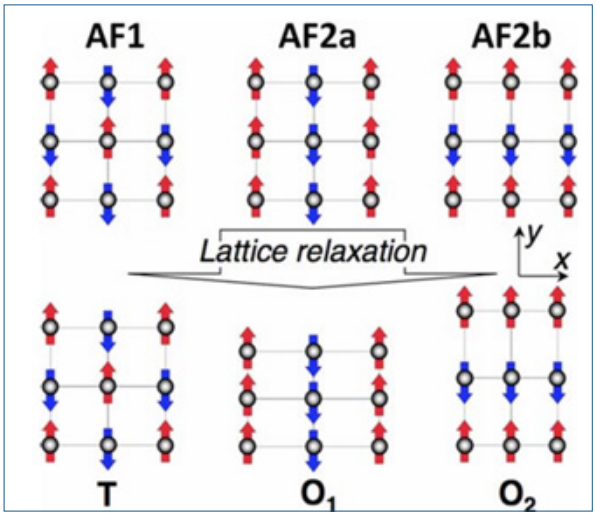


Figure 5: The upper images represent checkerboard type of spin pattern denoted AF1; and spin stripe type patterns denoted AF2a and AF2b spin configurations, in the tetragonal phase. Lower images represent the spin configurations of AF1, AF2a and AF2b in the orthorhombic.

Energies of the patterns are as follows.

$$E_{FM}\text{-}E_{AFM2} = 0.40 \text{ eV} \quad (1)$$

$$E_{AFM1}\text{-}E_{AFM2} = 0.15 \text{ eV} \quad (2)$$

This means that the energy ordering is

$$E_{FM} > E_{(AFM1)} > E_{(AFM2)} \quad (3)$$

Here

$$E_{(AFM2)} \equiv E_{(AFM2a)} = E_{(AFM2b)} \quad (4)$$

Potential energy surface in the orthorhombic phase in shown in Figure 6. Figure 6 (a) shows the potential energy surface is calculated for AF2a and AF2b spin configurations, with respective energy minima in orthorhombic structures O_1 and O_2. Arrows indicate spin-states of Fe 3d electrons for each branch of the potential energy surface, where the spin orientation is in the xy-plane with y-orientation. Figure 6 (b) shows the effects of temperature on the structural phase transition in stoichiometric LaFeAsO in an energy vs orientation plot. The magnetic order appears only at temperature below T_1.

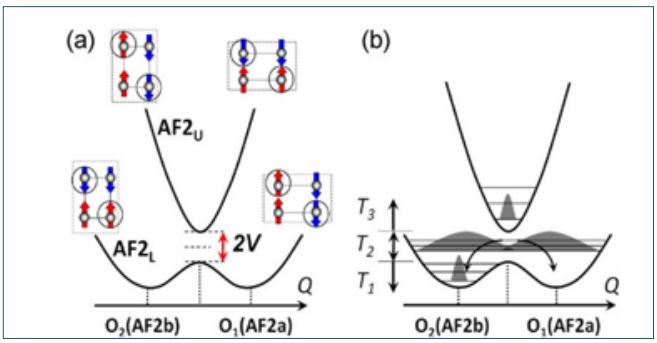


Figure 6: (a) Potential energy surface in an energy vs orientation plot calculated for AF2a and AF2b spin configurations, with respective energy minima in orthorhombic structures O_1 and O_2. Arrows indicate spin-states of Fe 3d electrons for each branch of the potential energy surface. (b) Temperature dependence shown in an energy vs orientation plot of the structural phase transition in stoichiometric LaFeAsO.

Moving on to the 122-type of pnictide, its crystal structure is seen in Figure 7. $BaFe_2As_2$ crystallizes in the tetragonal $ThCr_2Si_2$-type structure as listed in Table 1 [3,4] with two formula units per unit cell (space group I4/mmm, a = 3.9625 Å, c = 13.0168 Å, Z = 2) [5]. The crystal structure is easily described as layers formed by edge-sharing $FeAs_{4/4}$ tetrahedra perpendicular to [001], separated by Ba barium ions. A mirror plane is located between each layer in contrast to LaFeAsO, where each layer has the same orientation. The polar but covalent Fe −As bonds with bond length d_{Fe-As} = 2.403 Å, within the layers are the by far strongest ones, followed by the rather ionic Ba −As contacts with bond length d_{Ba-As} = 3.382 Å. Each barium atom has eight arsenic neighbors, which form a tetragonal prism. The distance of the arsenic atoms between the layers is separation distance d_{As-As} =3.788 Å, is much too long for any kind of interaction.

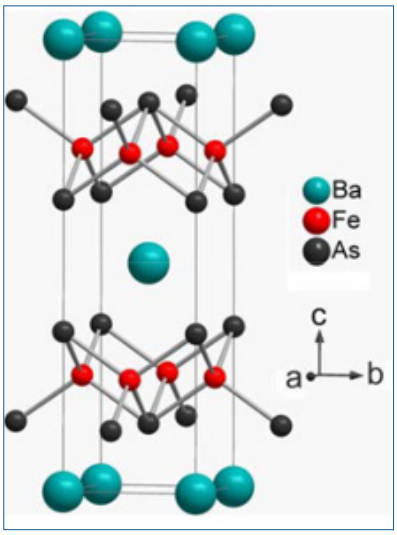


Figure 7: Crystal Structure of a Unit cell of $BaFe_2As_2$.

Metal-metal bonding within the layers plays an important role in the properties of $ThCr_2Si_2$-type compounds [6]. This is especially the in such compounds, where the Fermi level crosses the bands that originate from the direct ddσ- or ddπ-type overlap. Assuming the iron atoms are in the Fe_{2+} state (orbital state $3d^6$), the d-shell is more than half-filled and Fe−Fe anti-bonding states should be at least partially occupied. The lowest lying are the ddπ*-bands, made by the overlap of the Fe-$3d_{x2-y2}$ orbitals. Hence, the undoubtedly present Fe −Fe bonds with bond separation d_{Fe-Fe} = 2.802 Å in $BaFe_2As_2$ are slightly weakened, but more important, these bands are less dispersed and mainly responsible for the magnetic properties. $BaFe_2As_2$ is on the verge of a magnetic instability. Any change of the ddπ*-overlap (by larger or smaller Fe-Fe distances) will either broaden or flatten the d_{x2-y2} band, leading consequently to a nonmagnetic or magnetic state, respectively. By taking the chemical bonding into account, we have the typical Peierls-scenario, where the total energy can be lowered by a structural distortion, i.e. a reduction of symmetry. Thus, the magnetic and structural degrees of freedom are intimately coupled. These observations about the structural properties affecting the magnetic properties are focused on here because it is extremely important to not lose sight of the fact that both tetragonal and orthorhombic phases may harbor antiferromagnetic (AFM) behavior, and may be importantly related to engaging spin density wave (SDW) propagation in the lattice, a potential energy exchange mechanism contributing to superconductivity. In order to see this explicitly, inspect the potassium doped 122-type compound, plotted in Figure. 7.

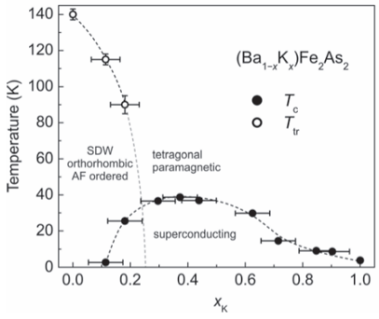


Figure 8: Phase Diagram of $Ba_{1-x}KxFe_2As_2$, with K Atom Doping of the Parent Compound.

One observes that there is a region K atom doping where it is a fraction below about 0.3, x_K = 0.3, when tetragonal crystal structure, spin density waves, and superconductivity, coexist. In fact, this SDW/SC coexistence is in the doping region,

$$0.10 < x_K < 0.25 \qquad (5)$$

and critical superconducting temperature may reach T_C = 32 K. But the highest T_C value occurs at about x_K = 0.4 .

Magnetic ordering in the unit cell crystal is shown in Figure 8. Neutron diffraction experiments of the solid solution $Ba_{1-x}K_xFe_2As_2$ showed a co-existence of magnetic ordering with superconductivity at doping levels x < 0.4 [8]. The structural distortion and magnetic ordering is completely absent already at x = 0.3 [9]. This discrepancy may be due to different preparation techniques.

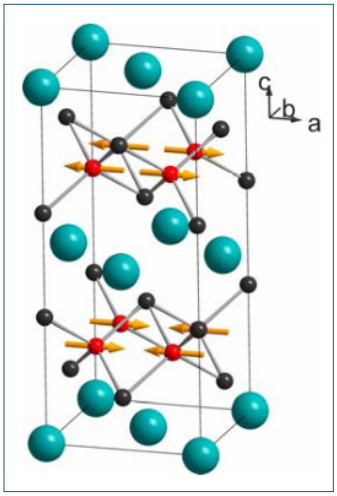


Figure 9: Magnetic Structure of $BaFe_2As_2$ Unit Cell Crystal. The Magnetic Moment is 0.87 μ_B /Fe.

Now look at the 111-type of pnictide superconductor LiFeAs. The structure of Li111 was determined by researchers using XRD on a single crystal with dimensions of ~ 0.28 x 0.14 x 0.02 mm^3 mounted in a glass fiber under a stream of cold nitrogen gas at -58 °C, using a Siemens SMART diffractometer [10]. Li111 crystallizes in a tetragonal structure (P4/nmm) of the anti- PbFCl-type with a = 3.7914(7) Å and c = 6.364(2) Å, as shown in Figure. 9. Li111 features Fe_2As_2 layers based on edge-sharing $FeAs_4$ tetrahedra or derived from As capping of the Fe-square nets, above and below each center of the 6 Fe-squares. The Fe-As bond distance d_{Fe-Fe} within the layer is d_{Fe-As} = 2.4204(4) Å; the nearest Fe-Fe distance is d_{Fe-Fe} = 2.6819(4) Å. The crystal, spin, and electronic structure of the "111"-type LiFeAs superconductor has been investigated by first-principles calculations based on the density-functional theory [11]. It is found that the crystal structure and weak magnetism of metallic LiFeAs can be described by general gradient approximation and local spin-density approximation (LSDA). Both methods show LiFeAs is a weak correlated system with a striped antiferromagnetic (AFM) ground state and the easy axis of magnetization is along the b direction of the magnetic unit cell. The magnetic unit cell is distorted from the tetragonal into an orthorhombic structure. The spin moment/Fe calculated by the LSDA method is $0.121\mu_B$.

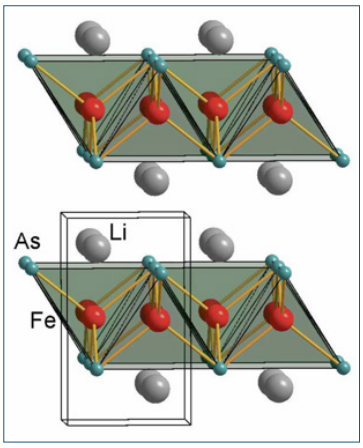


Figure 10: The 111-Type of Superconducting Pnictide LiFeAs Unit Cell Crystal Structure.

A major distinguishing feature is that, unlike "1111" (e.g., LaFeAsO) and "122" (e.g., $BaFe_2As_2$) families, stoichiometric 111-type of pnictide LiFeAs does *not* exhibit a spin-density wave (SDW) or antiferromagnetic ordering [12]. Research has indicated that LiFeAs may develop spontaneous nematic order (a breaking of rotational symmetry) within the superconducting state. The synthesis and properties of LiFeAs, a high-Tc Fe-based superconducting stoichiometric compound, indicate by single crystal x-ray studies that it crystallizes in the tetragonal PbFCl type (P4/nmm) with a = 3.7914(7) Å and c = 6.364(2) Å. Unlike the known isoelectronic undoped intrinsic FeAs compounds, LiFeAs does not show any spin-density wave behavior but exhibits superconductivity at ambient pressures without chemical doping. It exhibits a respectable transition temperature of T_C =18 K with electron-like carriers and a very high critical field, $H_{c2}(0)$ > 80 T. LiFeAs appears to be the chemical equivalent of the infinite layered compound of the high-T_c cuprates. The 11-type of pnictide is much simpler than the other pnictides, typified by FeSe, and its generic crystal structure is shown in Figure 11 [13]. In the figure, *Ch* denotes either Se or Te atoms. That is, *Ch* = Se, Te.

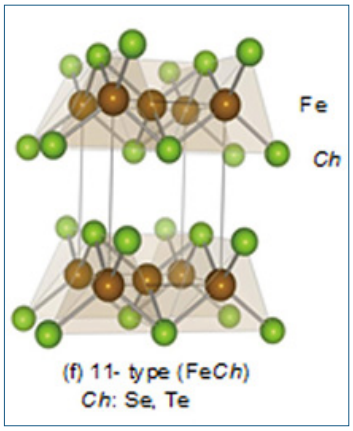


Figure 11: The 11-Type of Pnictide, Using Either Se or Te Atoms with iron Fe Atoms, Giving Either FeSe or FeTe.

More Complicated Pnictides

There are more complicated pnictide superconductors such as the 42622-type like $Ca_4Al_2O_6Fe_2As_2$, which when making a defect shortage of oxygen, giving superconductivity for $Ca_4Al_2O_{6-y}Fe_2As_2$, has a T_C = 28.3 K. A similar compound, replacing the As with P, yielding a defect structure of $Ca_4Al_2O_{6-y}Fe_2P_2$, has T_C = 17.1 K. Another more complicated pnictide compound of the type $(Fe_2As_2)(Ca_{n+1}(Mg,Ti)_nO_y)$ where n = 3, 4 and 9 ≤ y ≤ 10 was examined in [14] which seems to have T_C = 39 K. Figure 12 shows the crystal structure of (Fe_2As_2) $(Ca_5(Mg, Ti)_4O_y)$ where n = 4. The Fe_2As_2 part of the structure has a tetragonal cell with a space group of I4/mmm and consists FeAs layers. Oxide layers have a quadruple stack of perovskite cells. The lattice constants of this compound are a = 3.864(2) Å and c = 41.05(2) Å, giving it a unit cell crystal volume of

$$V_{tetragonal}^{unit\ cell:\ (Fe2As2)(Ca5(Mg,Ti)4Oy)} = a^2c = (3.864\ \text{Å})^2(41.02\ \text{Å}) = 612.45\ \text{Å}^3$$

Ionic radius of Ti^{4+} is $r_{ionic}^{Ti^{4+}}$ = 0.605 Å , which is smaller than that of Mg^{2+} $r_{ionic}^{Mg^{2+}}$ = 0.72 Å. Furthermore, the authors also found another even more complicated material of a somewhat different class, (Fe_2As_2) $(Ca_8(Mg, Ti)_6O_y)$, which is superconducting, with a sextuple of perovskite-like sheets divided by a rock salt layer. Interlayer Fe-Fe distance is about 30 Å.

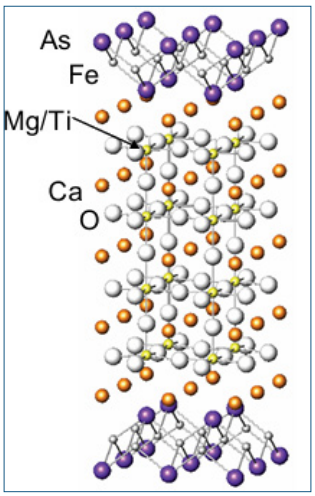


Figure 12: Crystal Structure of (Fe_2As_2) $(Ca_5(Mg, Ti)_4O_y)$.

Finally, a more general phase diagram for some of the 122-type of pnictides, is given in Figure 13 [15].

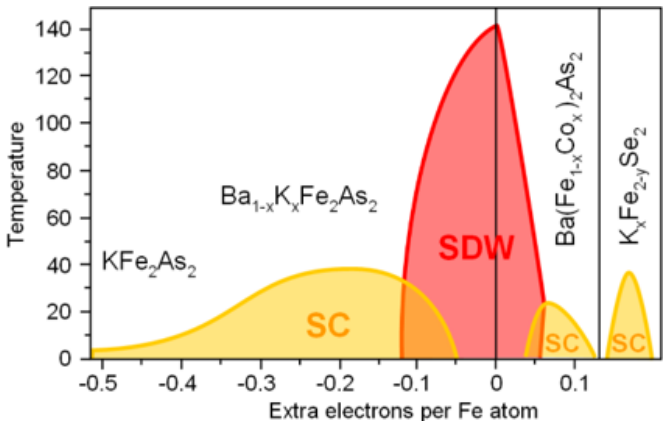


Figure 13: Some More General 122-Type of Pnictide Superconductors [15].

Cuprate Superconductors

Cuprate materials are what led the research community into the very high critical temperature realm. There are the Hg mercury based compounds like Hg-1223 $HgBa_2Ca_2Cu_3O_{8+\delta}$ with a T_C = 134 K and the simpler sister compound which is a Hg-1212

$HgBa_2CaCu_2O_{6+\delta}$ with a T_C = 104 K (with one less Cuplane, also reducing the Ca and Cu counts by one each) but with extra annealing T_C rise to 123 K, the Tl thallium based compounds like Tl-2223 $TlBa_2Ca_2Cu_3O_{10}$ with a T_C = 125 K, mixed Hg and Tl compounds which is still a (Tl, Hg)-2223 form with a (Tl1.6Hg0.4) with a T_C = 130 K, bismuth Bi based compounds like $Bi_2Sr_2Ca_2Cu_3O_{10}$ which is a Bi-2223 with a T_C = 110 K, and rare-earth based compounds like $YBa_2Cu_3O_7$ denoted YBCO with a T_C = 92 K. For $HgBa_2Ca_2Cu_3O_{8+\delta}$, its crystal structure is shown in Figure. 13 (a) [16,17]. One notices that only the barium Ba and calcium Ca atoms are fully contained within the unit cell. Mercury Hg is found at the top and bottom of the unit cell, so that each face contributes ½ of an atom of Hg. There are five internal oxygen O atom planes, and two faces containing O atoms at the top and bottom of the unit cell. End faces contribute ½ atom each, so for the two faces taken together 1/2×2 = 1, ,a total of 1 atom of O. Middle three planes containing O atoms, each contribute 2 atoms of O each, since each is a face atom of O, contributing ½ atom and there are 4 faces to the unit cell which each oxygen atom plane experiences, giving 1/2×4 = 2. Since there are three of these oxygen planes, this yields a total contribution to the oxygen count of 2×3 = 6. Then there are two planes containing oxygen atoms bracketed between the internal triplet of oxygen planes, and the end face mercury planes. Each of these planes has 4 atoms, each contributing 1/4 atom, giving 1/4×4 = 1 per plane. Because there are two of these bracketed planes, the total contribution from them is giving 1/4×4×2= 2. Finally, the top and bottom end faces of the unit cell, besides containing the mercury atoms, contain oxygen atoms. By inspection of Figure. 13, one is led to believe that each of the end faces contributes ½ atom, so the end faces contribute a total of 1/2×2= 1. This gives a total for all of the oxygen planes of 2+6+1=9. But this is not quite correct. However, with the end faces contributing a partial O atom because this is where it is expected the extra oxygen atom gets placed to modify the O atom stoichiometry to 8+δ, supposing just one face gets the extra O atom, the formula for the oxygen atom end face count becomes 1/2×1 + 0×1 = 1/2. This is very close to some of the observed values of δ = 0.4. In

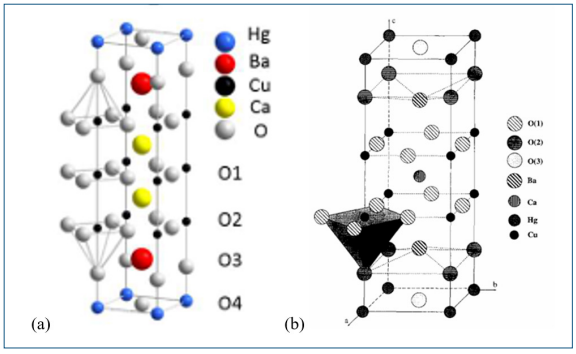


Figure 13: (a) Crystal structure of the cuprate superconductor $HgBa_2Ca_2Cu_3O_{8+\delta}$ unit cell [16,17]. Note that placement of an O atom on each end face is highly speculative and merely graphically suggestive, as the actual formula for end faces. (a) Crystal structure of the cuprate superconductor $HgBa_2CaCu_2O_{6+\delta}$ unit cell [18].

fact, the actual formula for the end faces is $f_{top}{}^{O}+f_{bot}{}^{O}=\delta$, where $f_{top}{}^{O}, f_{bot}{}^{O}$, are the fractional contributions of the top and bottom end faces to that oxygen count. This fractional breakdown is expected to vary on a random statistical basis from one unit cell to another, throughout the compound crystal, making the unit cell not quite a pure repetitive unit in the sample. Charge transport of the Cooper pairs is done by the planes holding the copper atoms. These are the three middle centered oxygen planes which one observes have 4 symmetrically placed Cu atoms. Each edge Cu atom in a plane contributes ¼ to the copper atom count, giving 1/4×4= 1. Since there are three planes, total copper atom count is 1/4×4×3= 3. One notices that per copper atom plane, one already knows the oxygen count is two O atoms, which yields an effective and widely recognized planar formula of CuO_2. The compound crystallizes with the symmetry of space group P4/mmm and lattice parameters a=3.8501(1) Å, c = 15.7837(9) Å. It has an oxygen composition corresponding to δ = 0.41, with this extra oxygen located on the layer of the mercury atoms at the end faces of the unit cell. The simpler sister compound $HgBa_2CaCu_2O_{6+\delta}$ has the symmetry of space group P4/mmm and lattice parameters a = 3.8526 (2)Å, c = 12.6367(8) Å with δ = 0.35, but with further annealing δ *is* lowered to δ = 0.28 and T_C raised by 19 K [18]. Other related studies are for $Hg_{1-x}Pb_xBa_2Ca_2Cu_3O_y$ (Figure. 13 (b)) [19]. The composition of this sample has been found experimentally and is specified by a formula of $Hg_{0.66}Pb_{0.34}Ba_2Ca_{1.98}Cu_{2.30}O_{8.4}$. Still another variant has a Tl substitution, $Hg_{0.8}Tl_{0.2}Ba_2Ca_2Cu_3O_{8+\delta}$, with the compound having the same crystal as Hg-1223 with the space group symmetry P4/mmm and lattice parameters a = 3.8489(1) Å, c = 15.816(1) Å [20]. Rietveld analysis results indicate that Hg is partially replaced by Tl, and the oxygen content, δ, is 0.33, with a T_C = 138 K.

Phase diagram of cuprate superconductors is shown in Figure. 14 can be roughly separated into electron (n) and hole (p) doped cuprates, somewhat like the models describing semiconductors. Both standard cuprate superconductors, YBCO and BSCCO, are notably hole-doped [21].

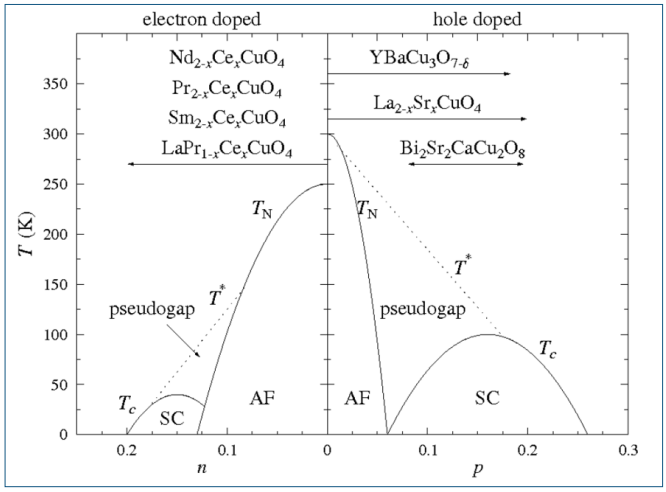


Figure 14: Phase Diagram of Cuprate Superconductors [20].

Other cuprate based superconductor crystal structures are shown in Figure 15. These include the cuprate superconductors La_2CuO_4, $YBa_2Cu_3O_7$, and $Bi_2Sr_2CaCu_2O_8$ provided by the Hirschfield group at the Univ. Florida [22]. La_2CuO_4 is the parent compound of the lanthanum-based high-temperature cuprate superconductors, thought of as an antiferromagnetic Mott insulator in its undoped state. It has a layered perovskite structure with CuO_2 planes. It becomes superconducting when doped with holes using Sr substitution or excess interstitial oxygen making $La_2CuO_{4+\delta}$. Superconductivity emerges when the trivalent ion La^{3+} is replaced by lower positive valence ions

such as the divalent ions Sr^{2+} or Ba^{2+} giving for example $La_{2-x}Sr_xCuO_4$ with a T_C = 40 K or $La_{2-x}Ba_xCuO_4$ [23]. In another study, three phases of the BSCCO superconductor are examined and show in Figure. 15 [24]. Highest critical temperatures for BSCCO compounds is a T_C =110 K. Crystal structures of BSCO-, BSCCO-, and BSCCO- type of cuprate superconductors of the 2201-, 2212-, and 2223-types are shown. Since Cu oxide superconductors have been discovered, the application for this type of BSCCO superconductor, especially in the form of superconducting tape to be used as electric cable to transport the electricity, was investigated. The aim to that study was to analyze the manufacture of superconducting wire with superconducting pellets as its precursor.

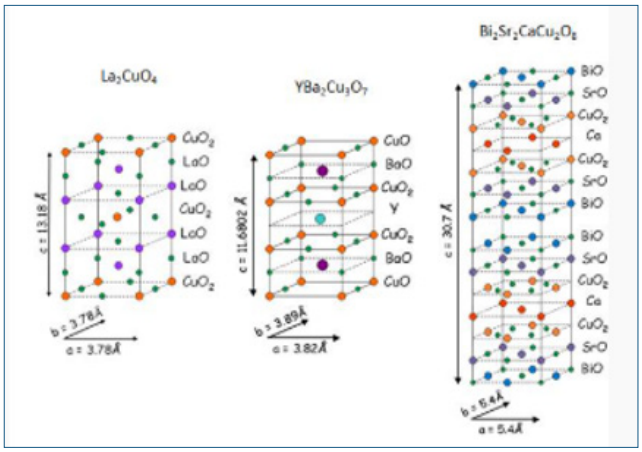


Figure 15: Crystal Structures of LCO-, YBCO-, and BSCCO-Type of Cuprate Superconductors [22].

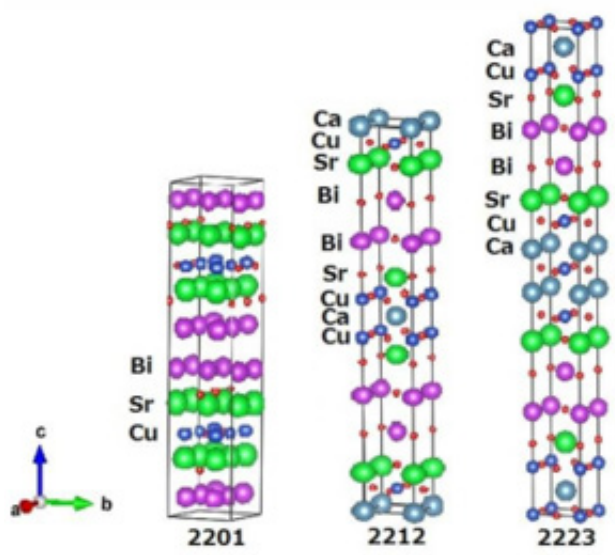


Figure 16: Crystal Structures of BSCO-, BSCCO-, and BSCCO-Type of Cuprate Superconductors of the 2201-, 2212-, and 2223-types [24].

Let's return to the LCO type of cuprate superconducting structures. Figure 16 shows the various crystal unit cell structures, of the T, T', and T* varieties.

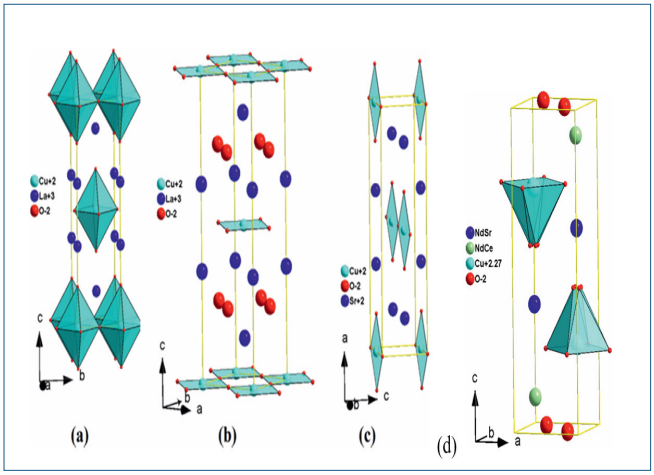


Figure 17: Structures of LCO cuprate superconductors: (a) T-La_2CuO_4, (b) T′-Nd_2CuO_4, (c) S-Sr_2CuO_3, and (d) T* - $Nd_{1.32}Sr_{0.41}Ce_{0.27}Cu_{03.93}$ [23].

The T-type structure relates to the La_2MO_4 system where M = Cu, Ni, and Co. At elevated temperatures, the La_2MO_4-type compounds correspond to the K_2NiF_4-type structure of tetragonal symmetry with the space group I4/mmm. The structure is described by the stacking, along the c-axis, of sheets of the MO_2 type separated from each other by double layers of the NaCl type or, by the stacking of the layers of octahedron MO6 of the perovskite-type which are translated relative to each other by (½, ½, and ½) and separated by La-O sheets of the NaCl type. The octahedra MO_6 is perfectly aligned with the c–axis; in case, HTT (high-temperature tetragonal) is ideal. At room temperature, the phases of the three systems: La_2CoO_4, La_2NiO_4, and La_2NiO_4, have an orthorhombic structure of the Bmab type called "low temperature orthorhombic" (LTO). The lengths of Map bonds vary according to the type of transition metal M; he Co–Oapical and Ni–Oapical bonds are equivalent, while the length of the Cu–Oapical bond is lengthened on the c-axis by the Jahn Teller effect due to the volume state of the Cu^{2+}. It is equal to 13.15 Å for La_2CuO_4 while it is between 12.55 Å and 12.70 Å for La_2CoO_4 and La_2NiO_4. The octahedra MO_6 is perfectly aligned with the c–axis; in case, HTT (high-temperature tetragonal) is ideal.

T′ type structure derives from that of the T type which results from a displacement of the apical oxygen atoms in the tetrahedral sites formed by the lanthanide ions, from where the layers of the NaCl type are replaced by layers of the fluorite type. The coordination number of Cu becomes 4 (square plane coordination) and that of Ln is 8 instead of 9. This structural transformation leads exclusively to a change in the coordination of the oxide; thus, the cation M is in square plane coordination, and the LnO_2 layers are of the fluorine type and no longer of the NaCl type. Crystal structure of the T′ phase can be described as an entanglement of fluorite ($Ln/O_2/Ln$) blocks with infinite shell blocks CuO_2. However, the space group remains the same for the 2 structures. The T* type structure consists of a stack of pyramids' layers (CuO_5) separated either by layers (LnO) of the NaCl type, or by layers of the fluorite type. As a result, this structure is intermediate between those of the T and T′ types. The stacking sequence of the atomic planes along the c-axis is A | B | A | C | A, with A: CuO_2, B: Ln–O_2–Ln, and C: LnO–LnO.

The Cu^{2+} cation is surrounded by five oxygen atoms, thus, forming a square-based pyramid while the Ln^{3+} cations are distributed in the coordination sites 9 and 8 in an ordered manner. Structure of the T* type phase is caused by thermodynamic competition between the chemical composition and pressure influencing the stability of the T and T′ phases. Due to this competition, the existence of this phase is extremely limited. The existence and presence of two ions Ln^{3+} and Ln'^{3+} of varied sizes cause the crystallization of the oxide of type $(Ln, Ln')_2CuO_4$ in the T* type structure. This is the case where Ln is La^{3+} and Ln′ is less voluminous ion such as Sm^{3+}, Eu^{3+}, Gd^{3+}, Dy^{3+}, and Tb^{3+}. The domain of the T*-type phase existence can be increased by the presence of a divalent cation with a large ionic radius such as Sr^{2+} which usually occupies the coordination site 9. Thus, the structure of the T* phase can include several oxides such as $(La, Ln, Sr)_2CuO_4$ and $(La, Ln')_2CuO_4$ (Ln = Sm, Eu, Gd, or Tb, and Ln′ = Dy, Tb, or Nd). The structure of the T* type phase has also a quadratic symmetry, and the space group of $Nd_{2-x-y}Ce_xSr_yCuO_{4-\delta}$ is P4/nmm for example.

The S-type structure is a model used mainly to describe oxygen-deficient compounds such as Ln_2CuO_{4-x} (Ln = Pr, Nd, Sm, Eu, Gd). Unlike T, T′ and T*, the S phase has oxygen vacancies at the equatorial sites, half of which are occupied. The oxygen vacancies are ordered such that Cu adopts a square planar coordination as shown in Fig. 17 (c). The copper atoms are surrounded by 2Oapical and 2Oequatorial instead of 4Oeq in the T′ phase. This is a major difference between the two phases S and T′ since the arrangement of CuO_4 square planes in the S-type structure does not form 2D layers, but 1D chains which share the following corners and orientations. The S-type phase has orthorhombic symmetry with a space group Immm.

Electron or hole doping has an influence on the antiferromagnetic order of CuO_2 planes. Doping is the operation that modifies the concentration of charge carriers in the CuO_2 planes. As mentioned above, there are two ways of doping the compound: either by substituting a cation with another of different valences, for example, in the $La_{2-x}Sr_xCuO_4$ system, the La^{3+} is substituted by Sr^{2+}, or simply by adding oxygen. In the undoped compounds, the planes adjacent to the CuO_2 planes consist of trivalent cations X^{3+}(La^{3+} in the phase La_2CuO_4 or Bi^{3+} for $Bi_2Sr_2CaCu_2O_8$). Only two of three electrons provided by X^{3+} are needed for bonding X^{3+} - O^{2-}. The electron remaining is transferred to blueprints $Cu^{2+}(O_2^-)_2$. The unit cell CuO2 takes an electron from the two neighboring layers XO, thus, ensuring electronic neutrality. However, when a divalent Z^{2+} ion is partially substituted for the trivalent X^{3+} ion, an electron deficit is created in the CuO_2 planes. This process can also be described as introducing holes in the copper-oxygen planes. These holes transform the $3d^9$ states of Cu^{2+} into Cu^{3+} (S = 0), and these ions represent a Cu^{2+} (S = ½) bonding state with a hole residing mainly in the four neighboring 2p orbitals of the oxygens that is called a "Zhang-Rice" singlet [25]. The introduction of hole-like charge carriers significantly alters the long-range antiferromagnetic ordering of the system as shown in Figure 18 (a), compared to that caused by introducing electron-like charge carriers Figure. 18 (b) [26].

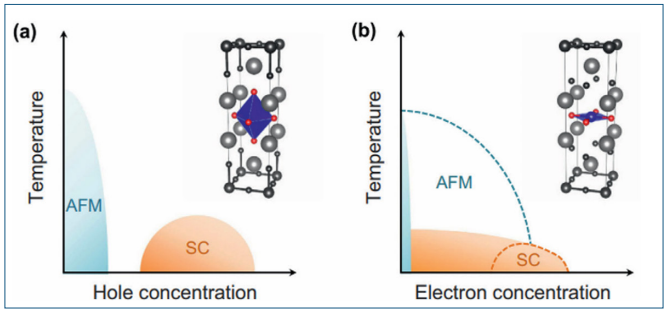


Figure 18: Schematic Representation of the Influence of (a) Hole or Electron (b) Doping on the Antiferromagnetic (AFM) Order of CuO_2 Planes [25].

Turn attention to the rare earth superconductor $YBa_2Cu_3O_7$ [27,28]. Its coordination geometry and unit cell crystal structure is given in Figure 19.

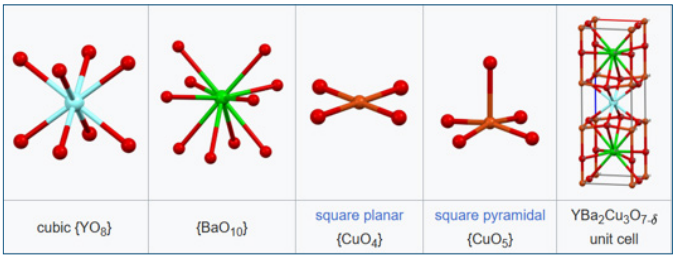


Figure 19: Coordination Geometry of Metal Centers in YBCO.

YBCO crystallizes in a defect perovskite structure. It can be viewed as a layered structure: the boundary of each layer is defined by planes of square planar CuO_4 units sharing 4 vertices. The planes can sometimes be slightly puckered. Perpendicular to these CuO_4 planes are CuO_2 ribbons sharing 2 vertices. The yttriumYatoms are found between the CuO_4 planes, while the bariumBaatoms are found between the CuO_2 ribbons and the CuO_4 planes, which is illustrated in Figure 20. The parent structure is not superconducting.

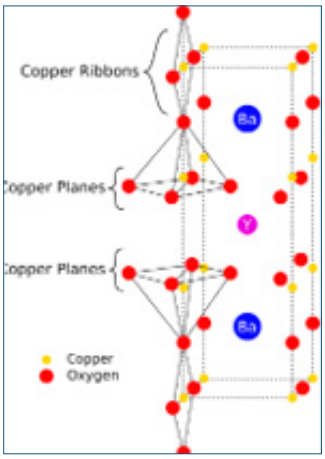


Figure 20: Part of the Lattice Structure of Yttrium Barium Copper Oxide YBCO.

A way is needed to provide charge carriers, and this is done by defect under doping oxygen, which alters the YBCO formula $YBa_2Cu_3O_{7-x}$. Optimum superconducting properties are found for x = 0.07, with a T_C = 95 K, and the structure is orthorhombic, with lattice constants a = 3.82 Å, b = 3.89 Å, and c = 11.68 Å

[29]. Interestingly, when x = 1, one gets the formula $YBa_2Cu_3O_6$ which is tetragonal. Superconducting feature displays itself as long as $0 \leq x \leq 0.65$. Conductivity is mainly confined to the *a-b* planes and a large anisotropy in transport properties is observed. Along the *c* axis, normal conductivity is 10 times smaller than in the *a-b* plane. Superconducting length scales show similar anisotropy, in both penetration depth, $\lambda_{ab} \approx 150$ nm, $\lambda_c \approx 800$ nm, and coherence length, $\xi_{ab} \approx 2$ nm, $\xi_c \approx 0.4$ nm. Although the coherence length in the *a-b* plane is 5.3 times greater than that along the *c* axis, it is quite small compared to classic superconductors such as niobium with $\xi_{Nb} \approx 40$ nm. Compared to Nb, with $\xi_{Nb}/\max\{\xi_{ab}, \xi_c\} = 20$, the YBCO superconducting state is much more sensitive to defects.

Magnesium Diboride Superconductor

Magnesium diboride is a binary superconductor with a simple, layered crystal structure that shares similarities with graphite [30]. Discovered as a superconductor in 2001, its critical temperature T_C = 39 K and is the highest among conventional (phonon-mediated) superconductors [31]. The structure of is classified as the hexagonal AlB_2-type (space group P/mmm). It consists of alternating layers of magnesium and boron. The boron layers form a flat, two-dimensional honeycomb, graphite-like, lattice with each boron atom covalently bonded to three others within the plane. The magnesium layers form a triangular lattice positioned halfway between the boron planes with each magnesium atom sitting at the center of a hexagonal prism formed by boron atoms. Unit cell crystal lattice parameters area = 3.08 Å , c = 3.52 Å . Figure 21 shows a sketch of MgB_2 crystal structure [30,32]. There is some indication that this material may possess two superconducting gaps [33].

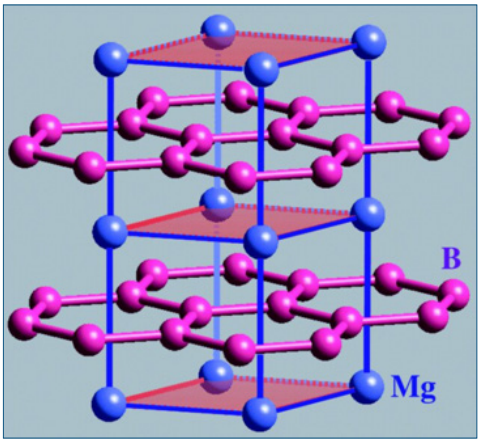


Figure 21: Superconductor MgB_2 Crystal Structure.

The Gap Parameter Δ and Its Relation to T_C

Although our main interest is to find crystal structures which exhibit very high critical superconductor temperatures T_C, there is nothing which prohibits us from wondering about the superconducting gap Δ. And even if somehow determining how to enhance its properties so as to yield much elevated T_C, is a route which could eventually yield insights on how to improve T_C. The approach works with the many-body Green's functions; the ordinary Green's function $G_{\uparrow\uparrow}(\mathbf{k},\tau)$, where **k** is the 3D momentum and τ is the imaginary Matsubara time frame, and the anomalous Green's function $F_{\downarrow\uparrow}(\mathbf{k},\tau)$ [34,35]. These two types of many-body Green's functions are related by a pair of equations of motion, giving the variation of the particular Green's function in Matsubara imaginary time, with a correcting quantity, proportional to the product of a gap parameter $\Delta_{\mathbf{k}}$ which is **k** dependent and the other Green's function. Furthermore, one knows that the BCS mean field Hamiltonian, which may be a rough proxy for us here to model the effects, consists of an energy diagonal term in terms of the fermion raising $c^{\dagger}_{\mathbf{k},\sigma}$ and lowering $\mathbf{c}_{\mathbf{k},\sigma}$ operators, and a Hermicity term (really two terms which when added maintain Hermiticity) which has opposing momentum and spin operators; namely $c^{\dagger}_{\mathbf{k},\sigma=\uparrow}$ and $c^{\dagger}_{-\mathbf{k},\sigma=\downarrow}$ for the raising operators, hit by the momentum gap parameter $\Delta_{\mathbf{k}}$. By an integration technique involving a complex valued function with poles in the complex z-plane, gap parameter can be related the overall exchange energy of all of the mechanisms, call it V^{RPA}_{eff} , where the superscript reminds us that this arose from a random phase approximation (RPA) [36,37].

$$\Delta_{\mathbf{k}} = V^{RPA}_{eff} \sum_{\mathbf{k}}^{|\xi_{\mathbf{k}'}|<\omega_D} \Delta_{\mathbf{k}} \frac{1 - f(\beta E_{\mathbf{k}})}{2E_{\mathbf{k}}} \tag{6}$$

Here $f(\beta E_k)$ is the Fermi-Dirac statistical function, withthe inverse thermal energy based on the ambient temperature *T*, $\beta = 1/(k_B T)$, where the Boltzmann constant is $k_B = 8.617 \times 10^{-5}$ eV/K. This makes the argument in *f* unitless. The sum in (6) is very non-trivial, as the gap is not only momentum dependent in **k**-space, but it may resolve into being both k magnitude and ***k*** direction dependent (that is possessing anisotropy). Also $\boldsymbol{E}_k$ is

$$E_{\mathbf{k}} = \sqrt{(\xi_{\mathbf{k}})^2 + |\Delta_{\mathbf{k}}|^2} \tag{7}$$

Complicated relationship (6) considerably simplifies if the limit when momentum independence occurs, is adopted.

$$\Delta_{\mathbf{k}} \to \Delta \tag{8}$$

In this situation, (6) becomes

$$\Delta = V^{RPA}_{eff} \sum_{\mathbf{k}}^{|\xi_{\mathbf{k}'}|<\omega_D} \Delta \frac{1 - f(\beta E_{\mathbf{k}})}{2E_{\mathbf{k}}} \tag{9}$$

Clearly, Δ can be extracted out of the summation, and divided out from both sides of the equation. The result is

$$1 = V^{RPA}_{eff} \sum_{\mathbf{k}}^{|\xi_{\mathbf{k}'}|<\omega_D} \frac{1 - f(\beta E_{\mathbf{k}})}{2E_{\mathbf{k}}} \tag{10}$$

Summation in (10) may be converted into an integral,

$$1 = V^{RPA}_{eff} D(\xi_{\mathbf{k}} \to 0) \int_{-\omega_D}^{\omega_D} \frac{\tanh\left[\frac{\beta}{2}\sqrt{(\xi_{\mathbf{k}})^2 + |\Delta|^2}\right]}{2\sqrt{(\xi_{\mathbf{k}})^2 + |\Delta|^2}} d\xi_{\mathbf{k}} \tag{11}$$

In (11), $\xi_{\mathbf{k}}$ is the diagonal Hamiltonian energy element measured relative to the Fermi energy. Density of states function in the limit is simply that at the Fermi level,

$$D(\xi_{\mathbf{k}} \to 0) = D(\varepsilon_F) \tag{12}$$

This gives the number of states per unit energy in the sample. Equation (11) is a transcendental relationship without an easy analytical solution. There are two aspects of (11) which make it hard to solve. First is the temperature dependence of β, which let's explicitly identify as

$$\beta = \frac{1}{k_B T} \tag{13}$$

which is embedded in the tanh function of (11). The second

not so obvious problem is with the transcendental nature of the equation itself. This makes the gap parameter highly temperature dependent,

$$\Delta_{\mathbf{k}} = \Delta_{\mathbf{k}}(T) \tag{14}$$

Once ω_D, V_{eff}^{RPA}, and $D(\xi_{\mathbf{k}} \to 0)$ are selected for a particular superconducting material, equation (11) generates a half parabolic solution, which near T=0 has a value $\Delta_0 = \Delta(0)$ with a slope approaching zero, $d\Delta(T)/dT|_{T\to 0} = 0$, and at T_C, $\Delta(0) = 0$.

Therefore, let us study what happens as the ambient temperature approaches zero, acquiring $\Delta_0 = \Delta(0)$ .The hyperbolic tanh function reduces to unity, as shown below, as one can see by examining its expression using exponentials.

$$\tanh(x) = \frac{1 - e^{-2x}}{1 + e^{-2x}} \tag{15}$$

Taking the limit as x→∞,

$$\lim_{x\to\infty} \tanh(x) = \lim_{x\to\infty} \frac{1 - e^{-2x}}{1 + e^{-2x}} = 1 \tag{16}$$

Of course, in our actual case, one replaces x by β', where β' is defined as

$$\beta' = \beta\sqrt{(\xi_{\mathbf{k}})^2 + |\Delta|^2}/2 \tag{17}$$

Limiting process in (11) takes the form then,

$$\begin{aligned}
1 &= V_{eff}^{RPA} D(\xi_{\mathbf{k}} \to 0) \lim_{T\to 0} \int_{-\omega_D}^{\omega_D} \frac{\tanh\left[\frac{\beta}{2}\sqrt{(\xi_{\mathbf{k}})^2 + |\Delta|^2}\right]}{2\sqrt{(\xi_{\mathbf{k}})^2 + |\Delta|^2}} d\xi_{\mathbf{k}} \\
&= V_{eff}^{RPA} D(\xi_{\mathbf{k}} \to 0) \lim_{\beta'\to\infty} \int_{-\omega_D}^{\omega_D} \frac{\tanh[\beta']}{2\sqrt{(\xi_{\mathbf{k}})^2 + |\Delta|^2}} d\xi_{\mathbf{k}} \\
&= V_{eff}^{RPA} D(\xi_{\mathbf{k}} \to 0) \int_{-\omega_D}^{\omega_D} \frac{\lim_{\beta'\to\infty} \tanh[\beta']}{2\sqrt{(\xi_{\mathbf{k}})^2 + \lim_{T\to 0}|\Delta|^2}} d\xi_{\mathbf{k}} \\
&= V_{eff}^{RPA} D(\xi_{\mathbf{k}} \to 0) \frac{1}{2} \int_{-\omega_D}^{\omega_D} \frac{1}{\sqrt{(\xi_{\mathbf{k}})^2 + |\Delta_0|^2}} d\xi_{\mathbf{k}} \\
&= V_{eff}^{RPA} D(\xi_{\mathbf{k}} \to 0) \int_{0}^{\omega_D} \frac{1}{\sqrt{(\xi_{\mathbf{k}})^2 + |\Delta_0|^2}} d\xi_{\mathbf{k}} \\
&= V_{eff}^{RPA} D(\xi_{\mathbf{k}} \to 0) \sinh^{-1}\left(\frac{\xi_{\mathbf{k}}}{|\Delta_0|}\right)\Big|_0^{\omega_D}
\end{aligned} \tag{18}$$

Since $\sinh^{-1}(0) = 0$, using (12), our final result is

$$1 = V_{eff}^{RPA} D(\varepsilon_F) \sinh^{-1}\left(\frac{\omega_D}{|\Delta_0|}\right) \tag{19}$$

This is another transcendental equation. It may be assessed by assigning a value to the inverse sinh function acting on its argument, which has embedded in it the gap parameter. Let

$$A = \frac{1}{V_{eff}^{RPA} D(\varepsilon_F)} \tag{20}$$

then

$$\sinh(A) = \frac{\omega_D}{|\Delta_0|} \Rightarrow \frac{1}{2}[e^A - e^{-A}] = \frac{\omega_D}{|\Delta_0|} \tag{21}$$

This expression may be inverted to determine to as

$$|\Delta(T=0)|_{mod\ str\ coup} = \frac{\omega_D}{\sinh(A)} \Rightarrow |\Delta(T=0)| = 2\omega_D \frac{1}{e^A - e^{-A}} =$$

$$2\omega_D \frac{1}{e^{\frac{1}{V_{eff}^{RPA} D(\varepsilon_F)}} - e^{-\frac{1}{V_{eff}^{RPA} D(\varepsilon_F)}}} \tag{22}$$

In (22) the assignment of gap parameter to the null temperature limit is explicitly indicated to alert one to this restriction. As long as $\Delta(T)$ has weak temperature dependence, this should pose no problem. In the weak coupling limit when the exchange energy V_{eff}^{RPA} is small measured against the inverse density of states $1/D(\varepsilon_F)$, that is when

$$V_{eff}^{RPA} D(\varepsilon_F) \ll 1 \tag{23}$$

(22) reduces to

$$|\Delta(T=0)|_{weak\ coupling} = 2\omega_D\, e^{-\frac{1}{V_{eff}^{RPA} D(\varepsilon_F)}} \tag{24}$$

because the second exponential in the numerator of (22) goes to zero. For the situation when one is hoping for much larger exchange energies V_{eff}^{RPA} due to multiple mechanisms contributing together, (24) is at most a rough approximation, and (22) should be used for a more accurate determination of the gap parameter. Equation (24) says that in the weak coupling limit,

$$\frac{|\Delta(T=0)|_{weak\ coupling}}{2\omega_D} \ll 1 \tag{25}$$

And that one expects $|\Delta(T=0)|_{weak\ coupling}$ to be small in terms of eV.

The moderate or strong coupling cases can be related to the weak coupling limit result in (24) by factoring out the appropriate exponential. The process is as follows.

$$|\Delta(T=0)|_{mod\ str\ coup} = 2\omega_D \frac{e^{-\frac{1}{V_{eff}^{RPA} D(\varepsilon_F)}}}{1 - e^{-\frac{2}{V_{eff}^{RPA} D(\varepsilon_F)}}} =$$

$$\frac{1}{1 - \frac{1}{2\omega_D}|\Delta(T=0)|_{weak\ cou}} |\Delta(T=0)|_{weak\ cou} \tag{26}$$

This equation shows what is happening. As $|\Delta(T=0)|$ leaves the realm of being small and enters the moderate or largeenergy gap region, in the denominator the second term knocks off an appreciable part from unity, upscaling the original $|\Delta(T=0)|_{weak\ cou}$, effectively giving the gap two factors hitting each other. Expressions (24) and (26) show that a powerful renormalization of the energy scale of the interaction occurs by using the exponential $exp[-1/\{V_{eff}^{RPA} D(\varepsilon_F)\}]$, which provides a completely non-perturbative form. This is because there exists no Tayler expansion of the function exp[-1/x], as x→0, which is precisely the weak coupling limit. Furthermore, no matter what the coupling strength, weak, moderate, or strong, once one approaches the lower side of the critical temperature

T_C, that is once one has $T_C \to T_C^-$, one expects and observes superconductivity vanishing. This vanishing can only occur if the superconducting gap also vanishes. Thus,

$$\Delta(T)|_{T\to T_C^-} = 0^+ \tag{27}$$

It is not possible to cross a phase transition zone by perturbation approaches using their expansions, since on either side of the line or surface crossed, two entirely different states of matter exist, which can not be connected by analytic continuation.

Knowing this, the critical temperature is acquired by returning to (11), and considering the limit as $T \to T_C$.

$$\begin{aligned}
1 &= V_{eff}^{RPA} D(\xi_{\mathbf{k}} \to 0) \lim_{T\to T_C^-} \int_{-\omega_D}^{\omega_D} \frac{\tanh\left[\frac{\beta}{2}\sqrt{(\xi_{\mathbf{k}})^2 + |\Delta|^2}\right]}{2\sqrt{(\xi_{\mathbf{k}})^2 + |\Delta|^2}} d\xi_{\mathbf{k}} \\
&= V_{eff}^{RPA} D(0) \int_{-\omega_D}^{\omega_D} \frac{\tanh\left[\frac{\lim_{T\to T_C^-}\beta}{2}\sqrt{(\xi_{\mathbf{k}})^2 + \lim_{T\to T_C^-}|\Delta|^2}\right]}{2\sqrt{(\xi_{\mathbf{k}})^2 + \lim_{T\to T_C^-}|\Delta|^2}} d\xi_{\mathbf{k}} \\
&= V_{eff}^{RPA} D(0) \int_0^{\omega_D} \frac{\tanh\left[\frac{1}{2k_B T_C}\xi\right]}{\xi} d\xi \\
&= V_{eff}^{RPA} D(0) \int_0^{\frac{\omega_D}{2k_B T_C}} \frac{\tanh[\xi']}{\xi'} d\xi' \\
&= V_{eff}^{RPA} D(0) \int_0^{\frac{\omega_D}{2k_B T_C}} \tanh[y] d(\ln[y])
\end{aligned} \tag{28}$$

Reason why the last equality in (28) was converted to that possessing a logarithmic differential, is to set up for an integration by parts which can retain a logarithmic form in at least one term. This allows a connection back to exponentials seen in (24) and embedded in (26).

Integration by parts yields for the last integral in (28),

$$\int_0^{y_u} \tanh[y] d(\ln[y]) = \{\tanh[y]\}(\ln[y])|_0^{y_u} - \int_0^{y_u} \ln[y] d(\tanh[y]) \tag{29}$$

where the upper integral limit is defined as

$$y_u = \frac{\omega_D}{2k_B T_C}$$

It is easy to observe that one has indeed captured a first term logarithmic factor in (29), as desired. Let us define our integral as

$$I(y_u) = \int_0^{y_u} \tanh[y] d(\ln[y]) = I_1(y_u) + I_2(y_u) \tag{30}$$

and write out its two parts as

$$I_1(y_u) = \{\tanh[y]\}(\ln[y])|_0^{y_u}; I_2(y_u) = -\int_0^{y_u} \ln[y] d(\tanh[y]) \tag{31a), (31b)}$$

Since the $\tanh[y]$ function is zero for the null lower integral limit, one obtains

$$I_1(y_u) = \{\tanh[y_u]\}(\ln[y_u]) \Rightarrow I_1 = \left\{\tanh\left[\frac{\omega_D}{2k_B T_C}\right]\right\}\left(\ln\left[\frac{\omega_D}{2k_B T_C}\right]\right) \tag{32}$$

In the weak coupling limit when $2k_B T_C$ may be small compared to the energy scale of the energy exchange interaction, that is when

$$y_u^{weak\ coup} = \frac{\omega_D}{2k_B T_C} \gg 1 \tag{33}$$

one may be induced to write for the first integral term

$$I_1^{weak\ coup}(y_u) = \ln\left[\frac{\omega_D}{2k_B T_C}\right] \tag{34}$$

By realizing $\tanh[y_u]$ is the hyperbolic tanh function of a large argument, which is nearly unity for $y_u \to \infty$.. For the case of moderate or strong coupling where inequality (33) is violated, which perhaps might begin to fail at $T_C \approx 50$ K because the factor of two in the denominator of the test ratio rescales that T_C to nearly $T_C^{rescaled} \approx 100$ K, which is in the region of the very high T_C values seen for the cuprate superconductors. For the cuprate superconductors, things are even worse, where T_C rescales to $T_C^{rescaled} \approx 200$ K Thus, for moderate or strong coupling cases, form (32) must be retained.

$$I_1^{mod/str\ coup}(y_u) = \left\{\tanh\left[\frac{\omega_D}{2k_B T_C}\right]\right\}\left(\ln\left[\frac{\omega_D}{2k_B T_C}\right]\right) \tag{35}$$

The second integral term in (29), seen in (31b), may be written out as

$$-I_2(y_u) = \int_0^{y_u} (\ln[y])(\mathrm{sech}^2[y]) dy = \int_0^{y_u} (\ln[y])(\cosh^{-2}[y]) dy \tag{36}$$

This definite integral can be evaluated on a value-by-value basis by varying the upper limit y_u . However, for the weak coupling limit, again taking $y_u \to \infty$, the integral reduces to a known form tabulated in a table of integrals. The result is

$$\int_0^{\infty} (\ln[y])(\cosh^{-2}[y]) dy = \ln\left[\frac{\pi}{4}\right] - C_{Euler} \tag{37}$$

as found in [37]. Here C_{Euler} is the Euler constant, defined by the formula,

$$C_{Euler} = \lim_{s\to\infty}\left(\sum_{m=1}^{s} \frac{1}{m} - \ln(s)\right) \tag{38}$$

Gradshteyn and Ryzhik provide the Euler constant to 24 places, which is provided here for completeness.

$$C_{Euler} = 0.577\ 215\ 664\ 901\ 532\ 860\ 606\ 512 \cdots \tag{39}$$

In formula (37), π to 20 places is

$$\pi = 3.141\ 592\ 653\ 589\ 793\ 238\ 46 \tag{40}$$

making

$$\ln\left[\frac{\pi}{4}\right] = -0.241\ 564\ 475\ 270\ 490\ 444\ 69 \tag{41}$$

In the weak coupling limit, then second integral is

$$-I_2^{weak\ coup} = \ln\left[\frac{\pi}{4}\right] - C_{Euler} \quad (42)$$

Convert (28) equation for determining T_C to

$$1 = V_{eff}^{RPA} D(0)\left[I_1^{weak\ coup} + I_2^{weak\ coup}\right] \quad (43)$$

Substitute in (34) and (42), obtaining

$$1 = V_{eff}^{RPA} D(0)\left[\ln\left[\frac{\omega_D}{2k_B T_C}\right] - \ln\left[\frac{\pi}{4}\right] + C_{Euler}\right] \quad (44)$$

Consolidating all of the right-hand-side terms into one logarithm,

$$1 = V_{eff}^{RPA} D(0)\left[\ln\left[\frac{\omega_D}{2k_B T_C}\frac{4}{\pi}e^{C_{Euler}}\right]\right] \quad (45)$$

Solution to (45) is

$$k_B T_C^{weak\ coup} = \frac{2}{\pi} e^{C_{Euler}} \omega_D e^{-\frac{1}{V_{eff}^{RPA} D(\varepsilon_F)}} \quad (46)$$

For moderate or strong coupling, one can find the correction or difference between the weak coupling limit integral $I_2^{weak\ coup}$ and the moderate or strong coupling integral. This difference is

$$\Delta I_2^{mod/str\ to\ weak\ coup} = I_2^{mod/str\ coup}(y_u) - I_2(y_u \to \infty) \quad (47)$$

or

$$\Delta I_2^{mod/str\ to\ weak\ coup}(y_u) = -\int_0^{y_u} (\ln[y])(\cosh^{-2}[y])dy - \ln\left[\frac{\pi}{4}\right] + C_{Euler} \quad (48)$$

For economy of expression notation, denote this difference as

$$C_{corr}^{mod/str}(y_u) = \Delta I_2^{mod/str\ to\ weak\ coup}(y_u) \quad (49)$$

Employing (49), with (28), (35)

$$1 = V_{eff}^{RPA} D(0)\left[I_1^{mod/str\ coup}(y_u) + I_2^{mod/str\ coup}(y_u)\right]$$
$$= V_{eff}^{RPA} D(0)\left[\left\{\tanh\left[\frac{\omega_D}{2k_B T_C}\right]\right\}\left(\ln\left[\frac{\omega_D}{2k_B T_C}\right]\right) - \ln\left[\frac{\pi}{4}\right] + C_{Euler} + C_{corr}^{mod/str}(y_u)\right] \quad (50)$$

It is very apparent that to perform a logarithmic absorption process as before, in anology to the weak coupling derivation, one would do well to define a scale factor b as

$$b = b(y_u) = \tanh[y_u] = \tanh\left[\frac{\omega_D}{2k_B T_C}\right] \quad (51)$$

Then (50) can be written as

$$1 = bV_{eff}^{RPA} D(0)\left[\left(\ln\left[\frac{\omega_D}{2k_B T_C}\right]\right) + \frac{1}{b}\left\{-\ln\left[\frac{\pi}{4}\right] + C_{Euler} + C_{corr}^{mod/str}(y_u)\right\}\right] \quad (52)$$

One may group all of the curly bracketed terms together, as before, obtaining

$$1 = bV_{eff}^{RPA} D(0)\left[\left(\ln\left[\frac{\omega_D}{2k_B T_C}\right]\right) + \frac{1}{b}\ln\left\{\frac{4}{\pi}e^{C_{Euler}} e^{C_{corr}^{mod/str}(y_u)}\right\}\right]$$
$$= bV_{eff}^{RPA} D(0)\left[\left(\ln\left[\frac{\omega_D}{2k_B T_C}\right]\right) + \ln\left\{\left(\frac{4}{\pi}\right)^{1/b} e^{C_{Euler}/b} e^{C_{corr}^{mod/str}(y_u)/b}\right\}\right]$$
$$= bV_{eff}^{RPA} D(0)\left\{\ln\left[\frac{\omega_D}{2k_B T_C}\left(\frac{4}{\pi}\right)^{1/b} e^{C_{Euler}/b} e^{C_{corr}^{mod/str}(y_u)/b}\right]\right\} \quad (53)$$

This equation may be inverted to obtain $2k_B T_C$ seen embedded inside the logarithm. Do this in two stages to observe the consequences of having imperfections introduced by the b scaling outside the logarithmic operator and inside of it.

First pull out the energy exchange scaling hitting the ln [ ] operator, getting

$$e^{\frac{1}{bV_{eff}^{RPA} D(0)}} = \frac{\omega_D}{2k_B T_C}\left(\frac{4}{\pi}\right)^{1/b} e^{C_{Euler}/b} e^{C_{corr}^{mod/str}(y_u)/b} \quad (54)$$

Next take the inverse logarithm of both sides of (54),

$$e^{\frac{1}{bV_{eff}^{RPA} D(0)}} = \frac{\omega_D}{2k_B T_C}\left(\frac{4}{\pi}\right)^{1/b} e^{C_{Euler}/b} e^{C_{corr}^{mod/str}(y_u)/b} \quad (55)$$

At this point in the derivation, multiply both sides of (55) by $k_B T_C$ and divide by the left-had-side exponential, to find

$$k_B T_C^{mod/str\ coup} = \frac{\omega_D}{2}\left(\frac{4}{\pi}\right)^{1/b} e^{C_{Euler}/b} e^{C_{corr}^{mod/str}(y_u)/b} e^{-\frac{1}{bV_{eff}^{RPA} D(0)}} \quad (56)$$

One sees that the factor b rescales the leading $4/\pi$ factor, the Euler exponential, the correction exponential, and the energy exchange exponential. Thus, moderate or strong coupling can significantly affect the outcome for determining the critical superconducting temperature.

Proposing Some Possible Alternative High T_C Crystal Structures

Now that examination of various crystal structures has occurred for previous moderate to high T_C crystal structures, and one has also considered how to express T_C and Δ analytically, it behooves us to consider what crystal structures might in the future provide a pathway to reaching a more room temperature like critical temperature. The crystal structure should capture the capability to enlist phonon, charge density waves, or spin density waves, seen to be active or potentially active in the cuprates (all the 3 mentioned), pnictides (possibly spin density waves and phonons), MgB_2 (phonons). The question is can one embed one crystal type with at least one energy exchange mechanism into another crystal type with another or other energy exchange mechanisms, to allow some type of additive energy exchange process? This would only work if the net total combined crystal structures had only a small increase in volume, while allowing an increase in energy exchange mechanisms. Obviously, under high pressure, this might be possible, but is not a viable alternative for room

temperature and pressure conditions (standard conditions) which is required for realistically technologically feasible manufacture and economic conditions. Let's see if one can diagrammatically using block objects, posit some new superconducting material crystal structures. Examine our first try, Figure 21.

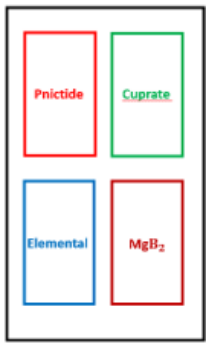


Figure 22: A Super Unit Crystal Cell Created Using Four Basic Classes of Superconducting Materials, the Pnictides, Cuprates, Elemental, and Simple Compounds (e.g., MgB_2).

Figure 22, has four of the basic classes of superconducting materials, the pnictides, cuprates, elemental, and simple compounds (e.g., MgB_2). By the implied construction of our super unit crystal unit cell, one suspects what is shown here is not merely four fundamental classes of superconducting materials, but also the framework for making metamaterial superconductors. Metamaterials have been used extensively in microwave and millimeter and smaller wavelength structures, to construct what is perhaps best characterized as metamaterial electromagnetic structures [39-54]. This has also been done for optical structures and devices [39]. If one wants each of the four classes of superconductors embedded inside a larger material structure, to retain their individual repetitive characteristics obtained from bulk like measurements, then enough repetitive unit cells must exist in 3D. Lert's suppose this number is ten. Then the super unit cell displayed in Figure. 22, morphs into that seen in Figure. 23.

Although the repetitive number shown in Figure. 23 is N_{rep} = 10, the choice is up to the material designer. And obviously, due to limitations of the graphic, only shown is the repeating unit cells in the x-direction, with appropriate indexing in that one dimension. If one had more space in this 2D diagram, one would repeat in the y-direction. But it is also understood that repeats occur in the z-direction of depth into the paper. Next Fig. 24, improves upon Fig. 23, by showing the repeating unit cells in the y-direction too. Indices attached to each unit cell shows its location in the xy-space. Indexing in each surface coordinate direction takes its index up to the maximum count N_{rep} = 10. Because it is now done for the xy-space, indexing is given as a numbered pair, (i, j) with $1 \le i, j \le N_{rep}$. In Figure 23, the paired indices used are (1, 1), (1, 10), (10, 1), and (10, 10).

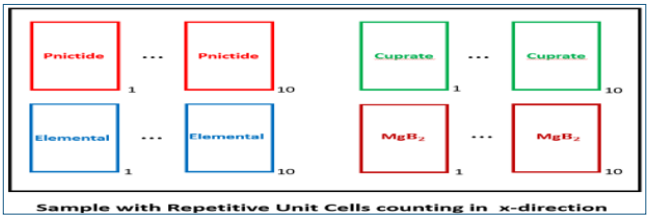


Figure 23: A Sample with Enough Repetitive Unit Crystal Cells to Create Bulk-Like Superconductive Regions, Using Four Basic Classes of Superconducting Materials, the Pnictides, Cuprates, Elemental, and Simple Compounds (e.g., MgB_2).

Although the repetitive number of unit cells was taken as 10, one can make a more physical based argument using concepts of coherence length and penetration depth. Earlier when looking at the rare earth superconductive material YBCO, superconducting length scales were shown to display anisotropy, in both the penetration depth, $\lambda ab \approx 150$ nm, $\lambda c \approx 800$ nm, and coherence length, $\xi ab \approx 2$ nm, $\xi c \approx 0.4$ nm. So, one discerns a single characteristic length scale for either coherence length or penetration depth is not realistic. First one must decide which length scale is the most appropriate one to use when marching off distance in any of the three coordinate directions, in order to create a bulk-like collection of the specific superconductor. Clearly, that length scale must be the coherence distance, which relates to Cooper pair entanglement. The other characteristic scale, the penetration depth, has to do with magnetic fields being able to enter or penetrate into the superconductor from an environment external the sample. That is obviously not what one wants to assess in terms of creating a bulk-like particular superconductor material. This is

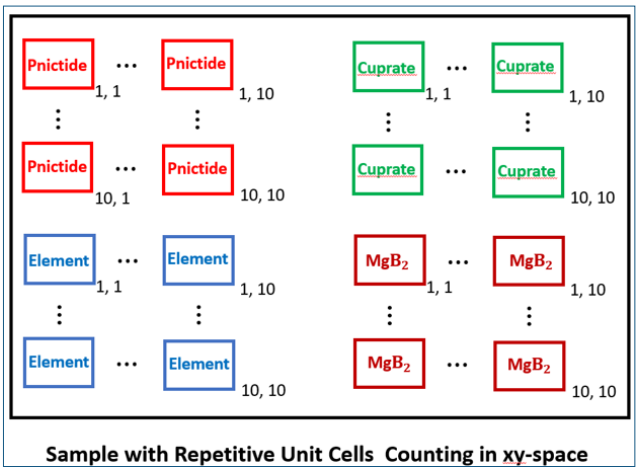


Figure 24: A Sample with Enough Repetitive Unit Crystal Cells to Create Bulk-Like Superconductive Regions, Using Four Basic Classes of Superconducting Materials, the Pnictides, Cuprates, Elemental, and Simple Compounds (e.g., MgB_2). Repetitive Unit Cells are Shown in the xy-space, indexed up to the Maximum Count imax, jmax =Nrep, which is 10 here.

good, because one notices that the ratio of the two scales can be very large,

$$\frac{penetration\ depth}{atom\ length\ scale} = \frac{\lambda_{pen}}{\xi_{coher}} = \frac{800\ nm}{0.4\ nm} = 2000 \qquad (57)$$

Here values were chosen so as to show how extreme the ratio can be, namely using the largest penetration depth and the smallest coherence distance. Also learned is that the typical penetration distance is huge compared to the length scale of an atom, which is for argument's sake taken as about 2 Å . That is, their ratio can be as extreme as

$$\frac{penetration\ depth}{atom\ length\ scale} = \frac{\lambda_{pen}}{l_{atom}} = \frac{800\ nm}{0.2\ nm} = 4000 \qquad (58)$$

However, ratio of coherence distance to the atom length scale, can be

$$\frac{\xi_{coher}|_{smallest}}{l_{atom}} = \frac{0.4\ nm}{0.2\ nm} = 2 \qquad (59)$$

this small. On the other hand, using the other extreme for coherence length,

$$\frac{\xi_{coher}|_{largest}}{l_{atom}} = \frac{2\ nm}{0.2\ nm} = 10 \qquad (60)$$

One recognizes immediately that (56) agrees with our prior choice of $N_{rep} = 10$.

If one wishes to create an actual metamaterial superconductor, which displays new properties based upon each class of superconductors utilized in the metamaterial structure, then the designer must arrange to have the various classes of superconductors talk to one another. This can be accomplished by choosing distances between the classes utilized, to encroach on the coherence lengths.

$$d_{sep\ bet\ classes}^{type\ 1\ SC-type\ 2\ SC} < min\{\xi_{coh}^{type\ 1\ SC}, \xi_{coh}^{type\ 2\ SC}\} \qquad (61)$$

$$d_{i,sep\ bet\ classes}^{type\ 1\ SC-type\ 2\ SC} < min\{\xi_{i,coh}^{type\ 1\ SC}, \xi_{i,coh}^{type\ 2\ SC}\} \quad ; i = x, y, z \qquad (62)$$

The astute reader will recognize that the rectangular coordinates do not necessarily align with the various crystal structure axes, which are measured by the lattice parameters a, b, and c, with the crystal structure determining in which direction the crystal axes march off in with respect the rectangular axes. That problem will be sidestepped for the moment. Rather, let us upgrade the structure shown in Fig. 23 to include these class separation distances, $d_{i,sep\ bet\ classes}^{type\ 1\ SC-type\ 2\ SC}$,indicated by the left-hand-side of (62).

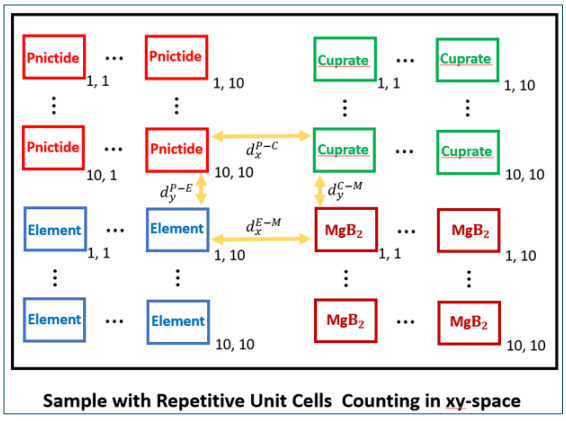


Figure 25: A Sample with Enough Repetitive Unit Crystal Cells to Create Bulk-Like Superconductive Regions, Using Four Basic Classes of Superconducting Materials, the Pnictides, Cuprates, Elemental, and Simple Compounds (e.g., MgB_2). Distances Between Various Classes of Superconductors is Shown in the more Central Part of the Diagram, and they Depend on the Coordinate Direction/Crystallographic Axis Directions.

Next question to answer is what might the critical temperature of the metamaterial composite superconductor be? There are basically two possibilities. That shown in (61) giving the condition for different superconductor class separations less than the relevant coherence lengths. And that when the separations exceed the coherence lengths. The latter condition is stated as

$$d_{sep\ bet\ classes}^{type\ 1\ SC-type\ 2\ SC} > max\{\xi_{coh}^{type\ 1\ SC}, \xi_{coh}^{type\ 2\ SC}\} \qquad (63)$$

Let us address the last condition first. For that situation, each class of superconductor retains their bulk like independent characteristics, including their T_C property, in the metamaterial composite. One might naively think that the composite critical temperature is a volume average, considering each partial superconducting class, $class_i$, weighting its particular $T_C^{class_i}$, where i = SC type = C_j, P_j, E_j, M_j, where the count in each particular class j varies from class to class, by its volume V_{class_i}.

$$T_{C;d>\xi}^{composite} \neq \sum_{i}^{N_{class}} \frac{V_{class_i}}{V_{tot}} T_C^{class_i} \qquad (64)$$

In (64) it is shown that this equation cannot hold, simply because whichever superconductive class of material has the lowest $T_C^{class_i}$, will set the maximum limit on the unobstructed superconductive flow of Cooper pairs. Thus, the correct composite T_C will be

$$T_{C;d>\xi}^{composite} = min\{T_C^{class_i};\ i = \text{SC type} = Cj, Pj, Ej, Mj,\} \qquad (65)$$

However, for different superconductor class separations less than the relevant coherence lengths, interactions between the various superconductor classes will occur, and so that type of metamaterial composite superconductor will not display any particular individual T_C^{classi}, but rather one based upon the interactions between the classes.

$$T_{C;d<\xi}^{composite} = \sum_{i,j}^{N_{class}} f\left(\frac{V_{class_i}}{V_{tot}}, d_{i,j}\right) T_C^{class_i} \qquad (66)$$

Where $d_{i,j}$ are the class separations, and the functions $f\left(\frac{V_{class_i}}{V_{tot}}, d_{i,j}\right)$ are complicated interaction functions dependent on each class of superconductor talking to one another through their coherence lengths.

Conclusions

In this work, various superconductive material crystal structures have been examined, from pncitides, to more complicated pnictides, to cuprate superconductor material crystal structures,

to magnesium diboride. Next the superconductive gap parameter Δ and its relation to the superconductive critical temperature T_C has been studied. It has been discovered tractable formulas still exist when going from low temperature superconductors with weak coupling to moderate and even strong coupling superconductors with much higher critical superconducting temperatures.In view of what one has learned, a first attempt at coming up with alternative superconducting structures has been attempted by referring back to earlier literature on metamaterials. Several possibilities have been discovered to make entirely new superconductor materials. These have been found to be divided into two distinct groups. The first group are those with specific classes of unit cell crystal structure regions which are in distant proximity to other different classes of unit cell crystal structure regions, all arranged in a metamaterial matrix. The second group are those with specific classes of unit cell crystal structure regions which are in close proximity to other different classes of unit cell crystal structure regions, all arranged in a metamaterial matrix. These two groups of metamaterial superconductors will have very different performances, including very different critical temperatures.

This paper has been a first attempt at breaking the seemingly insurmountable barrier of raising T_C within the realm of room temperature operation, so that economically viable power movement can occur on grid networks to bring power to various industries, communities, and other institutions such as hospitals. It might even become feasible to use such superconductive power grid lines to feed into storage batteries in a very efficient way.

References

1. Ni, N., Allred, J.M., Chan, B.C., Cava, R.J. (2011). High *Tc* electron doped $Ca_{10}(Pt_3As_8)(Fe_2As_2)_5$ and $Ca_{10}(Pt_4As_8)(Fe_2As_2)_5$ superconductors with skutterudite intermediary layers. Proceedings of the National Academy of Sciences, 108(45), E1019-E1026.
2. Nomura, T., Kim, S.W., Kamihara, Y., Hirano, M., Sushko, P.V., et al. (2008). Crystallographic phase transition and high-Tc superconductivity in LaFeAsO:F. Superconductor Science and Technology, 21(12), 125028.
3. Johrendt, D., Pöttgen, R. (2009). Superconductivity, magnetism and crystal chemistry of $Ba_{1-x}K_xFe_2As_2$. Physica c: superconductivity, 469(9-12), 332-339.
4. Ban, Z., Sikirica, M. (1965). The crystal structure of ternary silicides ThM_2Si_2 (M = Cr, Mn, Fe, Co, Ni and Cu). Acta Crystallographica, 18(4), 594-599.
5. Rotter, M., Tegel, M., Johrendt, D., Schellenberg, I., Hermes, W., et al. (2008). Spin-density-wave anomaly at 140 K in the ternary iron arsenide $BaFe_2As_2$. Physical Review B-Condensed Matter and Materials Physics, 78(2), 020503.
6. Johrendt, D., Felser, C., Jepsen, O., Andersen, O.K., Mewis, A., et al. (1997). LMTO band structure calculations of $ThCr_2Si_2$-type transition metal compounds. Journal of solid-state chemistry, 130(2), 254-265.
7. Huang, Q., Qiu, Y., Bao, W., Green, M.A., Lynn, J.W., et al. (2008). Neutron-diffraction measurements of magnetic order and a structural transition in the parent $BaFe_2As_2$ compounds of FeAs-based high-temperature superconductors. Physical Review Letters, 101(25), 257003.
8. Chen, H., Ren, Y., Qiu, Y., Bao, W., Liu, R. H., et al. (2009). Coexistence of the spin-density wave and superconductivity in $Ba_{1-x}K_xFe_2As_2$. EPL (Europhysics Letters), 85(1), 17006.
9. Rotter, M., Tegel, M., Schellenberg, I., Schappacher, F.M., Pöttgen, R., et al. (2009). Competition of magnetism and superconductivity in underdoped $(Ba_{1-x}K_x)Fe_2As_2$. New Journal of Physics, 11(2), 025014.
10. Chu, C.W., Chen, F., Gooch, M., Guloy, A.M., Lorenz, B., et al. (2009). The synthesis and characterization of LiFeAs and NaFeAs. Physica C: Superconductivity, 469(9-12), 326-331.
11. Li, Z., Tse, J.S., Jin, C.Q. (2009). Crystal, spin, and electronic structure of the superconductor LiFeAs. Physical Review B-Condensed Matter and Materials Physics, 80(9), 092503.
12. Tapp, J.H., Tang, Z., Lv, B., Sasmal, K., Lorenz, B., et al. (2008). LiFeAs: An intrinsic FeAs-based superconductor with *Tc*= 18 K. Physical Review B-Condensed Matter and Materials Physics, 78(6), 060505.
13. Mannella, N. (2014). The magnetic moment enigma in Fe-based high temperature superconductors. Journal of Physics: Condensed Matter, 26(47), 473202.
14. Ogino, H., Shimizu, Y., Kawaguchi, N., Kishio, K., Shimoyama, J.I., et al. (2011). A new iron pnictide oxide $(Fe_2As_2)(Ca_5(Mg,Ti)_4O_y)$ and a new phase in the Fe–As–Ca–Mg–Ti–O system. Superconductor Science and Technology, 24(8), 085020.
15. Kordyuk, A.A. (2012). Iron-based superconductors: Magnetism, superconductivity, and electronic structure. Low temperature physics, 38(9), 888-899.
16. Loret, B., Forget, A., Moussy, J.B., Poissonnet, S., Bonnaillie, P., et al. (2017). Crystal growth and characterization of $HgBa_2Ca_2Cu_3O_{8+\delta}$ superconductors with the highest critical temperature at ambient pressure. Inorganic Chemistry, 56(16), 9396-9399.
17. Chmaissem, O., Huang, Q., Antipov, E.V., Putilin, S.N., Marezio, M., et al. (1993). Neutron powder diffraction study at room temperature and at 10 K of the crystal structure of the 133 K superconductor $HgBa_2Ca_2Cu_3O_{8+\delta}$. Physica C: Superconductivity, 217(3-4), 265-272.
18. Antipov, E.V., Capponi, J.J., Chaillout, C., Chmaissem, O., Loureiro, S.M., et al. (1993). Synthesis and neutron powder diffraction study of the superconductor $HgBa_2CaCu_2O_{6+\delta}$ before and after heat treatment. Physica C: Superconductivity, 218(3-4), 348-355.
19. Shao, H.M., Lam, C.C., Fung, P.C.W., Wu, X.S., Du, J.H., et al. (1995). The synthesis and characterization of $HgBa_2Ca_2Cu_3O_{8+\delta}$ superconductors with substitution of Hg by Pb. Physica C: Superconductivity, 246(3-4), 207-215.
20. Dai, P., Chakoumakos, B.C., Sun, G.F., Wong, K.W., Xin, Y., et al. (1995). Synthesis and neutron powder diffraction study of the superconductor $HgBa_2Ca_2Cu_3O_{8+\delta}$ by Tl substitution. Physica C: Superconductivity, 243(3-4), 201-206.
21. Hartinger, C. (2009). DFG FG 538-Doping Dependence of Phase Transitions and Ordering Phenomena in Cuprate Superconductors. wmi.badw-muenchen.de. Archived from the original on 27 December 2008, https://www.socialresearchfoundation.com/new/publish-journal.php?editID=3931.
22. Hirschfield, P. (2026). web site, Univ. Florida.
23. Marzougui, B., Marzouki, A., Smida, Y.B., Marzouki, R. (2023). The Cuprate Ln_2CuO_4 (Ln: Rare Earth): Synthesis, Crystallography, and Applications. In Crystal Growth and Chirality-Technologies and Applications. IntechOpen,

https://www.intechopen.com/chapters/85541
24. Imaduddin, A., Hendrik, Dwi Yudanto, S., Nugraha, H., Sebleku, P., et al. (2018). Study on Cold-Drawing in Powder-in-Tube Process in Fabricating Silver-Sheathed (Bi,Pb)-Sr-Ca-Cu-O Tapes. In Journal of Physics: Conference Series 1091(1), 012004.
25. Akpojotor, G.E. (2008). Possible propagation of the Zhang–Rice singlet as a probable Cooper channel in the CuO_2 planes. Physics Letters A, 372(46), 6992-6995.
26. Jang, S.W., Sakakibara, H., Kino, H., Kotani, T., Kuroki, K., et al. (2016). Direct theoretical evidence for weaker correlations in electron-doped and Hg-based hole-doped cuprates. Scientific reports, 6(1), 33397.
27. Calestani, G., Rizzoli, C. (1987). Crystal structure of the $YBa_2Cu_3O_7$ superconductor by single-crystal X-ray diffraction. Nature, 328(6131), 606-607.
28. Williams, A., Kwei, G.H., Von Dreele, R.B., Raistrick, I.D., Bish, D.L. (1988). "Joint x-ray and neutron refinement of the structure of superconducting $YBa_2Cu_3O_{7-x}$: Precision structure, anisotropic thermal parameters, strain, and cation disorder," Phys. Rev. B. 37 (13), 7960-7962.
29. Mook, H.A., Yethiraj, M., Aeppli, G., Mason, T.E., Armstrong, T. (1993). Polarized neutron determination of the magnetic excitations in $YBa_2Cu_3O_7$. Physical review letters, 70(22), 3490.
30. Yildirim, T. (2002). The surprising superconductor. Materials today, 5(4), 40-44.
31. Nagamatsu, J., Nakagawa, N., Muranaka, T., Zenitani, Y., Akimitsu, J. (2001). Superconductivity at 39 K in magnesium diboride. Nature, 410(6824), 63.
32. Matera, D., Bonura, M., Černý, R., McKeown Walker, S., Buta, F., et al. (2020). High-field superconductivity in C-doped MgB_2 bulk samples prepared by a rapid synthesis route. Scientific reports, 10(1), 17656.
33. Souma, S., Machida, Y., Sato, T., Takahashi, T., Matsui, H., et al. (2003). The origin of multiple superconducting gaps in MgB_2. Nature, 423(6935), 65-67.
34. Fetter, A.L., Walecka, J.D. (1977). Quantum theory of many-particle systems.
35. Bruus, H., Flensberg, K. (2004). Many-body quantum theory in condensed matter physics: an introduction. Oxford University Press.
36. Krowne, C.M. (2017). Disorder Modifications of the Critical Temperature for Superconductivity: A Perspective from the Point of View of Nanoscience. In Advances in Imaging and Electron Physics, 202, 39-74.
37. Krowne, C.M. (2017). Critical Magnetic Field and Its Slope, Specific Heat, and Gap for Superconductivity as Modified by Nanoscopic Disorder. In Advances in Imaging and Electron Physics, 203, 67-97.
38. Gradshteyn, I.S., Ryzhik, I.M. (1980). Table of Integrals, Series, and Products, Academic Press, 4th edition, translated from Russian, 580, https://cir.nii.ac.jp/crid/1970023484908950180
39. Krowne, C.M., Zhang, Y. (2007). Editors of Physics of negative refraction and negative index materials. Optical and Electronic Aspects and Diversified Approaches. Springer-Verlag Berlin Heidelberg, https://link.springer.com/book/10.1007/978-3-540-72132-1.
40. Krowne, C.M. (2004). Physics of propagation in left-handed guided wave structures at microwave and millimeter-wave frequencies. Physical review letters, 92(5), 053901.
41. Krowne, C.M. (2003). Electromagnetic-field theory and numerically generated results for propagation in left-handed guided-wave single-microstrip structures. IEEE transactions on microwave theory and techniques, 51(12), 2269-2283.
42. Lakhtakia, A., Krowne, C.M. (2003). Restricted equivalence of paired epsilon–negative and mu–negative layers to a negative phase–velocity material (aliasleft–handed material). Optik, 114(7), 305-307.
43. Krowne, C.M. (2004). Negative-refractive bicrystal with broken symmetry produces asymmetric electromagnetic fields in guided-wave heterostructures. Physical review letters, 93(5), 053902.
44. Krowne, C.M. (2005). Left-Handed Materials for Microwave Devices and Circuits," Encyclopedia of RF and Microwave Engineering, Wiley, 3, 2303-2320.
45. Krowne, C.M. (2006). Left-handed material anisotropy effect on guided wave electromagnetic fields. Journal of applied physics, 99(4), 044914.
46. Krowne, C.M., Daniel, M. (2007). Electromagnetic Field Behavior in Dispersive Isotropic Negative Phase Velocity/Negative Refractive Index Guided Wave Structures Compatible with Millimeter-Wave Monolithic Integrated Circuits. Journal of Nanomaterials, 2007(1), 54568.
47. Krowne, C.M. (2007). Negative refractive heterostructure bicrystal for beam steering or control component action. Applied physics letters, 91(2), 022902.
48. Krowne, C.M. (2007). Low loss guided wave propagation in a left-handed microstrip structure using dispersive split ring–rod combination metamaterial. IET Microwaves, Antennas & Propagation, 1(4), 887-892.
49. Krowne, C.M. (2008). Multi-species two-level atomic media displaying electromagnetic left handedness. Physics Letters A, 372(13), 2304-2310.
50. Krowne, C.M. (2008). Anisotropy of electromagnetically induced left-handedness in atomic three-level media based upon bianisotropic polarizabilities and tensor character. Physics Letters A, 372(21), 3926-3933.
51. Krowne, C.M., Shen, J.Q. (2009). Dressed-state mixed-parity transitions for realizing negative refractive index. Physical Review A-Atomic, Molecular, and Optical Physics, 79(2), 023818.
52. Krowne, C.M. (2018). Obtaining Negative Index MetaMaterials Using Quantum States: Part I. Vacuum Tech. & Coating, 10, 41 - 48.
53. Krowne, C.M. (2010). Obtaining Negative Index MetaMaterials Using Quantum States: Part II. Vacuum Tech. & Coating, 10, 38-44.
54. Krowne, C.M. (2010). The Road to Quantum Level Negative Index MetaMaterials. J. Waves Random Complex Media 20, 223-250.

Copyright: ©2026 Clifford M Krowne. This is an open-access article distributed under the terms of the Creative Commons Attribution License, which permits unrestricted use, distribution, and reproduction in any medium, provided the original author and source are credited.